

# Forward Model Emulator for Atmospheric Radiative Transfer Using Gaussian Processes And Cross Validation

Otto Lamminpää<sup>1</sup>, Jouni Susiluoto<sup>1</sup>, Jonathan Hobbs<sup>1</sup>, James McDuffie<sup>1</sup>, Amy Braverman<sup>1</sup>, and Houman Owhadi<sup>2</sup>

<sup>1</sup>Jet Propulsion Laboratory, California Institute of Technology, Pasadena, CA, USA

<sup>2</sup>California Institute of Technology, Pasadena, CA, USA

**Correspondence:** Otto Lamminpää (otto.m.lamminpaa@jpl.nasa.gov)

**Abstract.** Remote sensing of atmospheric carbon dioxide (CO<sub>2</sub>) carried out by NASA's Orbiting Carbon Observatory-2 (OCO-2) satellite mission and the related Uncertainty Quantification (UQ) effort involves repeated evaluations of a state-of-the-art atmospheric physics model. The retrieval, or solving an inverse problem, requires substantial computational resources. In this work, we propose and implement a statistical emulator to speed up the computations in the OCO-2 physics model. Our approach is based on Gaussian Process (GP) Regression, leveraging recent research on Kernel Flows and Cross Validation to efficiently learn the kernel function in the GP. We demonstrate our method by replicating the behavior of OCO-2 forward model within measurement error precision, and further show that in simulated cases, our method reproduces the CO<sub>2</sub> retrieval performance of OCO-2 setup with orders of magnitude faster computational time. The underlying emulation problem is challenging because it is high dimensional. It is related to operator learning in the sense that the function to be approximated is mapping high-dimensional vectors to high-dimensional vectors. Our proposed approach is not only fast but also highly accurate (its relative error is less than 1%). In contrast with Artificial Neural Network (ANN) based methods, it is interpretable and its efficiency is based on learning a kernel in an engineered and expressive family of kernels.

*Copyright statement.* ©2024. California Institute of Technology. Government sponsorship acknowledged.

## 1 Introduction

Climate change, one of the most significant global environmental challenges, is primarily attributed to anthropogenic carbon emissions, which have accelerated the increase of carbon dioxide (CO<sub>2</sub>) in the atmosphere, posing a threat to Earth's future. The industrial revolution marked the onset of increased CO<sub>2</sub> emissions due to the extensive use of fossil fuels in various industries, such as transportation, manufacturing, and agriculture. The Intergovernmental Panel on Climate Change underscores CO<sub>2</sub>'s potent effect on planetary warming due to significant radiative forcing (IPCC, 2023). The atmospheric concentration of this trace gas is increasing at ever faster rate, and as of May 2023, the measured CO<sub>2</sub> at Mauna Loa station was 424.0 ppm, a 3 ppm increase from a year before (421.0 ppm in May 2022). Although the global terrestrial biosphere and oceans each take up about 25% of these emissions (Friedlingstein et al., 2022), this balance may not be sustainable, which might lead to unpredictable

feedbacks in the carbon cycle and the global climate system. These couplings between the Earth's climate system and the carbon cycle can introduce significant uncertainty in future climate change projections (Friedlingstein et al., 2014), which  
25 further renders mitigation efforts increasingly challenging.

For reliable climate modeling and future scenario prediction, it's crucial to estimate carbon flux accurately (e.g. Carbon-Tracker, Peters et al. (2007)), which involves quantifying both the sources and natural sinks of carbon. However, current *in situ* measurement networks are primarily deployed in the northern midlatitudes, leaving areas like the tropics underrepresented (Schimel et al., 2015). This lack of extensive coverage results in large uncertainties in flux estimates, underscoring the need for  
30 a more comprehensive global measurement network.

To provide a significant increase in coverage and resolution to the ground based data set, global estimates of total column averaged mole-fraction CO<sub>2</sub> (average amount of CO<sub>2</sub> over a vertical column of air in a specific ground pixel/location), denoted XCO<sub>2</sub>, are collected using satellite-borne spectrometers. These instruments include the Japanese Greenhouse gases Observing SATellite (GOSAT, Kuze et al. (2009)), operational since January 2009, follow-on GOSAT-2 (Imasu et al., 2023) launched in  
35 October 2018, the Orbiting Carbon Observatory-2 from NASA (OCO-2, Crisp et al. (2012)), launched in July 2014, and the OCO-3 instrument (Eldering et al., 2019) taken to the International Space Station May 2019, and the Chinese TanSat (Ran and Li, 2019) and TanSat 2 (Wu et al., 2023). Planned future missions include the Geostationary Carbon Cycle Observatory (GeoCarb, Moore III et al. (2018)), the European CO<sub>2</sub> Monitoring Mission (CO2M, Sierk et al. (2019)) and the Global Observing Satellite for Greenhouse gases and Water cycle (GOSAT-GW, Kasahara et al. (2020)). In this work, we focus exclusively  
40 on OCO-2, which, like all the above mentioned missions, measures solar radiance at the top of the atmosphere, reflected by Earth's surface and attenuated by atmospheric scattering and absorption by trace gases and aerosols. From these observed radiances, the OCO-2 mission uses a framework called *Optimal Estimation* (OE, Rodgers (2004)) to solve the related Bayesian inverse problem (see e.g. Kaipio and Somersalo (2005)), referred to as a retrieval. OE is an iterative algorithm, returning an estimate of posterior mean and covariance as a Gaussian approximation to the non-linear retrieval problem. Operationally the  
45 retrieval problem is solved using the Atmospheric Carbon Observations from Space (ACOS) software (O'Dell et al., 2018), which implements OE using a state-of-the-art atmospheric Full Physics model (FP). Processing OCO-2 measurements with the ACOS algorithm is a computationally intensive task, and currently about one-third of prescreened clear soundings are used in a low-latency data processing stream ((O'Dell et al., 2018)). As the data record grows, computational speed is also a major hindrance for retrospective processing of the full collection of cloud-free soundings for the current and any future improved  
50 algorithms. Thus, computational efficiency is a limiting factor in releasing the improved data to the user community. These issues are certain to get even worse with upcoming wider swath missions like CO2M and GOSAT-GW, as evidenced by another greenhouse gas imaging mission, Tropospheric Ozone Monitoring Instrument (TROPOMI, Veefkind et al. (2012)) from regularly reprocessing their data record, which is more than 20 times greater in size than that of OCO-2.

As with all inverse problems, some approximations and assumptions have to be made in the ACOS algorithm. The resulting  
55 XCO<sub>2</sub> estimates have to be validated and bias corrected using ground-based measurements from the Total Carbon Column Observing Network (TCCON, Wunch et al. (2017)), and COLlaborative Carbon Column Observing Network (COCCON, Frey et al. (2019)) as a reference. These sites are concentrated on the Northern Midlatitudes, and as a result of this coverage issue

and the imperfections in the FP model, significant systematic errors persist in the data set. (See e.g. Kiel et al. (2019) for effect of systematic errors, and Cressie (2018) for overview of statistical treatment of, and issues in the retrieval). Considerable effort has been exerted to tackle the high accuracy (less than 0.3 parts per million (ppm) in scenes with background levels of around 410 ppm), and high precision (standard errors less than 0.5 ppm) requirements of ingesting OCO-2 into flux inversion, which is the primary application of the data product. (Gurney et al. (2002), Patra et al. (2007), Liu et al. (2017), Palmer et al. (2019), Crowell et al. (2019), Peiro et al. (2022), Byrne et al. (2022)). Recent advancements of applying Markov Chain Monte Carlo (MCMC, Brynjarsdóttir et al. (2018), Lamminpää et al. (2019)) for non-Gaussian posterior characterization, and Simulation Based Uncertainty Quantification (Turmon and Braverman (2019), Braverman et al. (2021)) for capturing the overall uncertainty in the retrieval pipeline have been successfully deployed for addressing persisting retrieval errors. These methods, although comprehensive, suffer equally from computational speed issues as they require extensive amounts of FP evaluations.

Computational speed issues in OE retrievals have been attempted to address in several ways. Neural network (NN) based machine learning approaches (David et al. (2021), Mishra and Molinaro (2021), Bréon et al. (2022)) have been implemented to a combination of real world radiance data and model atmospheres (outputs of computational atmospheric models, like the Copernicus Atmospheric Monitoring Services (CAMS) model (Chevallier et al., 2010)). The OCO-2 forward model itself was sped up by using a surrogate model (Hobbs et al., 2017) that only partially considered the physical processes present in the FP model, and more recently by using a Gaussian Process (GP) emulator (Ma et al., 2019) for replicating the output of the FP model. In this paper, we will take similar approach using GPs, but with several improvements and an application to solving the retrieval problem with the help of closed-form Jacobians required in the gradient-based algorithm. GPs are a well-suited technique for forward model emulation, since they can be used with less data (130K (David et al., 2021) for NN vs. 20K for GP (see section 4)) and trained more quickly than NN based approaches. Additionally, a GP provides uncertainty estimates and closed-form Jacobians trivially, which are not straightforward to extract from a NN. For training efficiency, our approach will leverage recent novel techniques for GP parameter learning called *Kernel Flows* (Owhadi and Yoo, 2019), and training data generation via evaluating the FP model using the Reusable Framework for Atmospheric Composition (ReFRACtor) (McDuffie et al., 2018). We will demonstrate the accuracy of forward model emulation against a held out test set of FP evaluations, and further demonstrate the ability of our emulator to replicate the OE retrieval performance of ReFRACtor FP model in a fraction of computational time. Our approach achieves a remarkably low prediction error, less than 1% ("within measurement error limits"), which is an excellent result in the field of more general *operator learning*. Strategies to achieve learning more complicated operators, like the FP in our case, often involve a NN based architecture (Lu et al. (2021), Li et al. (2022)). Our approach follows the example set by Battie et al. (2023) that kernel methods are competitive in operator learning.

The rest of the paper is organized as follows. Section 2 will describe in detail the GP regression, kernel learning and resulting forward model emulator. Section 3 will further elaborate on the details of the OCO-2 retrieval algorithm, the state vector, and FP model describing atmospheric radiative transfer. Section 4 will detail the emulator implementation of ReFRACtor FP model and assess its performance. Section 5 will show results of our emulator used in a simulated XCO<sub>2</sub> retrieval context, and finally Section 6 will provide concluding remarks and ideas on future work and applications.

## 2 Gaussian Process Emulator

*Gaussian Process (GP) regression* (Rasmussen and Williams, 2006) (also called *kriging* in spatial context: Cressie (1993); Stein (1999)) is a well studied methodology for approximating any continuous function to an arbitrary accuracy, leveraging training data and a *kernel function* prescribed a priori. In addition, once trained, the GP model can be used to obtain fast and accurate predictions of a computationally demanding physics model, estimate prediction uncertainty, and compute closed-form derivatives and Jacobians for the prediction. Physical constraints like positive parameter values can be accounted for in training data design (which we address in later sections), so that predictions happen within the support of training data set. This is to say that our training data set will cover the expected minimum and maximum values of each parameter in the state vector. For example, surface albedo is physically restricted between 0 (no reflected light) and 1 (full reflection). If our training data is sufficiently well spread covering this range, we can make good predictions essentially by interpolation within the physically feasible interval. Potential departure from this support can be detected by large prediction uncertainty values, as the prediction uncertainty of a GP gets large by design if the input location doesn't have training points near it. In this section, we outline the basic theory of GP regression and outline our approach to modeling the continuous function between atmospheric state vectors  $\mathbf{x}$  and radiances  $\mathbf{y}$  observed by the OCO-2 instrument. We also provide background on Maximum Likelihood Estimation for fitting GP models, and present a novel root mean square error cross-validation extension for Kernel Flows (Owhadi and Yoo, 2019) approach, which we employ for the rest of this work.

### 2.1 Gaussian Process Regression

To construct an emulator for the forward model  $F(\mathbf{x})$ , we employ Gaussian Process (GP) regression to predict a *label*  $z^* \in \mathbb{R}$  at a new *state*  $\mathbf{x}^* \in \mathbb{R}^m$ . A GP is defined by a *kernel function* (defined explicitly later)  $k(x, x') : \mathcal{X} \times \mathcal{X} \rightarrow \mathbb{R}$ , where in the cases studied in this work  $\mathcal{X} = \mathbb{R}^m$ . We denote by  $\Gamma[\mathbf{X}, \mathbf{X}]$  the matrix of all kernel function evaluations over the training data  $\mathbf{X} \in \mathbb{R}^{m \times N}$  of  $N$  points with the entries  $\Gamma[\mathbf{X}, \mathbf{X}]_{i,j} = k(\mathbf{x}_i, \mathbf{x}_j)$  where  $\mathbf{x}_i, \mathbf{x}_j$  are the  $i$ th and  $j$ th training data points, respectively. Furthermore,  $\Gamma[\mathbf{x}^*, \mathbf{X}]$  denotes the vector of kernel evaluations of state  $\mathbf{x}^*$  against all training points  $\mathbf{X}$ . Using the training data together with vector of corresponding labels  $\mathbf{z} \in \mathbb{R}^N$ , a GP prediction of label (or function value) at a new state  $\mathbf{x}^*$  is given by

$$z^* \equiv GP(\mathbf{x}^*) = \Gamma[\mathbf{x}^*, \mathbf{X}](\Gamma[\mathbf{X}, \mathbf{X}] + \sigma\mathbb{I})^{-1}\mathbf{z}, \quad (1)$$

where we have assumed w.l.g. that the training data are centered and thus the GP has a zero mean. We add that the term  $(\Gamma[\mathbf{X}, \mathbf{X}] + \sigma\mathbb{I})^{-1}\mathbf{z}$  does not depend on the new input state, so it can be pre-computed. This makes the predictions take minimal computational time by avoiding inverting potentially large matrix  $(\Gamma[\mathbf{X}, \mathbf{X}] + \sigma\mathbb{I})^{-1}$ .

**Remark:** In GP literature, the variance term  $\sigma\mathbb{I}$  is usually taken to be the measurement error or local-scale unexplained variability in the training labels  $\mathbf{z}$ . However, since we are interested in reproducing the outputs of a computer code, the “measurements” are exact and hence there is no measurement error. It was shown in Owhadi and Yoo (2019) that learning the

parameters of GP models from noiseless data is can lead to unstable predictive models and numerical singularities. For this  
 125 reason, we treat  $\sigma$  as a regularization parameter, which captures the empirical mismatch between the model and the actual data,  
 and optimize it together with other kernel parameters.

In addition to point predictions, GP prediction can be associated with prediction uncertainty (the posterior variance of the  
 GP), given by

$$\sigma^* = k(\mathbf{x}^*, \mathbf{x}^*) - \mathbf{\Gamma}[\mathbf{x}^*, \mathbf{X}](\mathbf{\Gamma}[\mathbf{X}, \mathbf{X}] + \sigma\mathbb{I})^{-1}\mathbf{\Gamma}[\mathbf{x}^*, \mathbf{X}]^T. \quad (2)$$

130 The ability to include prediction uncertainties sets GP regression apart from many modern neural network based machine  
 learning methods, which only provide a point estimate as a prediction. Large prediction variance can be an indication of  
 departure from the support of training data set, indicating that GP is likely to lose its prediction skill. Additionally, uncertainty  
 from the predictions can be propagated forward and accounted for in further applications of a GP based emulators.

**Remark:** The GP formulas presented here rely on conditional Gaussian distributions, and thus has a similar structure to  
 135 that of Optimal Interpolation (OI; e.g., page 157 of (Kalnay, 2002)) and related iterative Optimal Estimation (OE) algorithms  
 (e.g., eq. 15), which both are widely used methods in atmospheric remote sensing. OI/OE use Gaussian assumptions to derive  
 a mean and covariance for the posterior distribution as a solution to an inverse problem, i.e. data assimilation or a retrieval. In  
 Gaussian Process Regression, the target function (here, the forward model) is represented similarly by a Gaussian distribution  
 that has a mean (prediction) and covariance (error estimate of the prediction).

140 Our interest will be in replicating the results of a gradient based optimization problem. Hence, in addition to fast evaluations  
 of  $F(\mathbf{x})$ , we would also benefit from fast derivatives obtained from closed form expressions. Combining equations (1) and (4),  
 we get

$$\frac{d}{d\mathbf{x}^*}z^* = \frac{d}{d\mathbf{x}^*}\mathbf{\Gamma}[\mathbf{x}^*, \mathbf{X}](\mathbf{\Gamma}[\mathbf{X}, \mathbf{X}] + \sigma\mathbb{I})^{-1}\mathbf{z}, \quad (3)$$

which describes taking the derivative of (1) wrt.  $\mathbf{x}^*$ .

145 **Remark:** While other machine learning methods, such as artificial neural networks and multilayer perceptrons, can in prin-  
 ciple be differentiated, computing the derivatives of a large architecture is computationally more demanding than evaluating  
 the expression 3, which motivates our use of GP regression. Other similar approaches, e.g. radial basis function networks, can  
 be shown to be universal approximators as well and could be used in place of GPs. As will be shown, our approach yields  
 a fast and accurate predictor that is intuitive and relatively easy to implement, so comparison against other machine learning  
 150 methods will not be pursued further in the scope of this work.

## 2.2 Kernel Function

A crucial modeling choice in GP regression is specification of a kernel function. This task involves either expert knowledge  
 of the domain structure, or some iterative trial and error search. In our application, we have empirically observed that a kernel  
 function consisting of sum of Matérn and linear kernels yields excellent predictive performance. This is likely due to a locally  
 155 near-linear behavior commonly assumed with the OCO-2 forward model being captured by the linear kernel, together with a

largely flexible Matérn term that is known to capture a large variety of non-linear effects. Matérn kernel is a more expressive choice of kernel compared to the usual Gaussian / radial basis functions used by default in Gaussian Process Regression, which tend to be "too smooth" to capture more abrupt changes in the function that is being approximated. Furthermore, such kernel can also be differentiated in closed form. The kernel function used throughout this work is given by

$$160 \quad k(\mathbf{x}, \mathbf{x}') = \alpha_1 \left( 1 + \frac{\sqrt{3}}{l} \|(\mathbf{x} - \mathbf{x}')\|_{\mathcal{W}} \right) \exp \left( -\frac{\sqrt{3}}{l} \|(\mathbf{x} - \mathbf{x}')\|_{\mathcal{W}} \right) + \alpha_2 (\mathcal{W}\mathbf{x})^T (\mathcal{W}\mathbf{x}') \quad (4)$$

where  $\|(\mathbf{x} - \mathbf{x}')\|_{\mathcal{W}} = \sqrt{(\mathbf{x} - \mathbf{x}')^T \mathcal{W}^2 (\mathbf{x} - \mathbf{x}')}$ ,  $\mathcal{W} = \text{diag}(\mathbf{w})$  is a diagonal matrix where  $\mathbf{w} \in \mathbb{R}^m$  is a vector of weights,  $l \in \mathbb{R}$  is a length scale parameter, and  $\alpha_1, \alpha_2 \in \mathbb{R}_+$  are positive weights that are restricted to sum to 1.

To compute Jacobians, we need an expression for the derivative of the kernel function  $\frac{d}{d\mathbf{x}^*} \Gamma[\mathbf{x}^*, \mathbf{X}]$  in expression 3. This can be computed in closed form from eq. (4) using known matrix identities. The derivation of a closed form expression can be  
 165 found in Appendix A.

### 2.3 Parameter Learning

Prediction quality of GP regression depends on identifying the hyperparameters  $\theta$  that best fit the training data. In our case, following the form of our kernel function, we have  $\theta = [\mathbf{w}, l, \sigma, \alpha_1, \alpha_2]$ . Hyperparameters are commonly learned via optimization, using maximum likelihood estimation (MLE, (Rasmussen and Williams, 2006)). This amounts to minimizing

$$170 \quad \mathcal{L}(\theta) = -\frac{1}{2} \log[\det \Gamma_{\theta}] - \frac{1}{2} \mathbf{z}^T \Gamma(\theta)^{-1} \mathbf{z}, \quad (5)$$

where  $\Gamma(\theta) = \Gamma[\mathbf{X}, \mathbf{X}]$  evaluated at parameter values  $\theta$ . Although this method is usually robust and performs well, GP applications with high dimensional inputs and large amount of training data are known to be challenging due to inverse matrix and log determinant calculations. Numerous approaches have been suggested to tackle this problem (e.g. local approximations (Vecchia, 1988), (Datta et al., 2016)). Inspired by the Kernel Flows approach (Owhadi and Yoo, 2019) where kernel parameters  
 175 are learned by minimizing a relative Reproducing Kernel Hilbert Space (RKHS) norm, we propose a cross-validation root mean square error based method to be used in this work. Intuitively, RKHS norm is a way, to measure the smoothness of a function approximation achieved with kernel method. While smooth methods generally yield discretization-invariant predictors, we propose to directly minimize the prediction error instead. The intuition of this approach is to iteratively select small mini-batches of the training data set, and individually leave points out one-by-one while using the rest of the mini-batch to predict  
 180 the left out values (via formula 1). Learning the kernel parameters that minimize this prediction error leads to globally good predictions given new inputs. This approach leverages the known screening effect associated with Matérn kernels, where the effects of far away points on prediction accuracy diminishes and only close-by points are necessary for prediction accuracy. The same intuition is the basis of numerous nearest neighbors GP methods (e.g. (Vecchia, 1988)). The upsides of our approach are the ability to select small mini-batches on each training iteration, allowing for faster computations while avoiding expensive  
 185 log-determinant calculations and inverting the large covariance matrices required in MLE. We will later show that our proposed method converges reliably and yields excellent predictions.

We start by selecting a mini-batch  $\mathbf{X}^{\text{Batch}}, \mathbf{z}^{\text{Batch}}$  of size  $N_{\text{Batch}}$  by randomly sampling from training data. We define a leave-one-out (LOO) cross-validation loss function with respect to  $L^2$  error (also known as root mean square error, RMSE) by first considering taking out one data point from the training data, and using the rest to predict it. This can be achieved by  
190 modifying the GP prediction formula from eq. (1) and leaving out the  $i$ th data point. This is achieved via a rank-one downdate  $\tilde{\mathbf{\Gamma}}(\theta)^{-1} - \frac{\tilde{\mathbf{\Gamma}}(\theta)^{-1} \tilde{\mathbf{\Gamma}}(\theta)_{:,i}^{-T}}{\tilde{\mathbf{\Gamma}}(\theta)_{i,i}^{-1}}$  to remove the effect of  $i$ th data point from the inverse covariance matrix  $\tilde{\mathbf{\Gamma}}(\theta)^{-1}$ . (See Stewart (1998) and Zhu et al. (2022) for details). The modified LOO prediction formula is then given by

$$\widetilde{GP}(\theta, i) = \tilde{\mathbf{\Gamma}}(\theta)_{:,i}^T \left( \tilde{\mathbf{\Gamma}}(\theta)^{-1} - \frac{\tilde{\mathbf{\Gamma}}(\theta)^{-1} \tilde{\mathbf{\Gamma}}(\theta)_{:,i}^{-T}}{\tilde{\mathbf{\Gamma}}(\theta)_{i,i}^{-1}} \right) \mathbf{z}^{\text{Batch}} \quad (6)$$

where  $\tilde{\mathbf{\Gamma}}(\theta) = \mathbf{\Gamma}(\mathbf{X}^{\text{Batch}}, \mathbf{X}^{\text{Batch}})$  is the  $N_{\text{Batch}} \times N_{\text{Batch}}$  covariance over the mini-batch evaluated at parameter values  $\theta$ . Here,  
205 the notation  $\tilde{\mathbf{\Gamma}}(\theta)_{:,i}$  means all rows of the  $i$ th column. We then define the final loss function by using formula (6) to predict  $z_i$  (the  $i$ th training label removed from the mini-batch) as

$$\rho(\theta) = \sum_{i=k_1}^{k_p} \left( \widetilde{GP}(\theta, i) - z_i \right)^2 + \epsilon \|\theta_0 - \theta\|^k, \quad (7)$$

where  $i \in [k_1 \dots k_p] \subset [1 \dots N_{\text{Batch}}]$  is a subset of  $p \leq N_{\text{Batch}}$  indices denoting elements of the mini-batch selected for prediction, which can be chosen as e.g. the entire mini-batch, or the  $p$  nearest neighbors of the center point of the mini-batch. The  
200 regularization term with error norm  $\|\cdot\|^2$ , some penalty magnitude  $\epsilon$ , and mean  $\theta_0$ , is included to ensure that kernel amplitude parameter values don't grow uncontrollably. This is done since we have observed empirically that letting non-identifiable parameters grow during optimization can lead to the optimizer getting "stuck", whereas this problem is not observed when regularizing the loss function. One may for example set  $\theta_0$  to be a vector of 1's.

We can now optimize the kernel parameters iteratively by repeatedly selecting mini-batches and updating  $\theta$  along  
205 the gradient of  $\rho(\theta)$ , which is obtained by automatic differentiation using Julia's *Zygote* package (Innes, 2018). We note that closed-form kernel derivatives could be used here as well, but since automatic differentiation with mini-batch sizes we use uses negligible computational time we won't pursue this idea further in this work. We note that as the mini-batch is selected at random, this method can be viewed as stochastic gradient descent. For this reason, we use the adaptive moment estimation (ADAM, (Kingma and Ba, 2017)) optimizer for finding the optimal value. Use of a momentum based optimizer is further  
210 recommended in this application as we have observed that the cost function often has several local minima. The optimization procedure is summarized in Algorithm 1. The final parameter value can be selected to be the one corresponding to the smallest loss function value achieved during training.

## 2.4 Training Data Generation

As we aim to reproduce the performance of a function represented as computer code, we take advantage of the freedom to use  
215 a space filling design for  $\mathbf{x}$  in  $\mathbb{R}^m$  for training data creation. We first span the unit cube  $[0, 1]^m$  with a *Sobol sequence* ((Sobol, 1967), (Press et al., 1992)) of  $N$  points. In practice we employ Julia's *Sobol.jl* (Johnson, 2020) package for this step. Then,

---

**Algorithm 1** Kernel Parameter Learning

---

**Input:** Kernel function  $k$ , training data  $(\mathbf{X}, \mathbf{z})$ , batch size  $N_{\text{Batch}}$ , number of prediction points  $p$ , number of iterations  $N_{\text{Iter}}$ .

**Output:** Matrix of kernel parameters  $\Theta$  and vector of loss values  $\mathbf{R}$

```
1: Initialize  $\theta_1 \leftarrow 1, \Theta \leftarrow \mathbf{0}, \mathbf{R} \leftarrow \mathbf{0}$ 
2: for all  $i$  in  $1 \dots N_{\text{Iter}}$  do
3:    $\mathbf{X}^{\text{Batch}} \leftarrow \mathbf{X}[\text{rand}(N_{\text{Batch}})], \mathbf{z}^{\text{Batch}} \leftarrow \mathbf{z}[\text{rand}(N_{\text{Batch}})]$            // Randomly select a mini-batch  $\mathbf{X}^{\text{Batch}}, \mathbf{z}^{\text{Batch}}$ 
4:    $\mathbf{R}[i] \leftarrow \rho(\theta_i)$                                                                                                      // Compute loss  $\rho(\theta_i)$  from (7)
5:    $\Theta[i] \leftarrow \theta_{i+1}, \theta_{i+1} \leftarrow \theta_i + \text{ADAM}(\frac{\partial}{\partial \theta} \rho(\theta_i))$  // Compute gradient  $\frac{\partial}{\partial \theta} \rho(\theta_i)$  and update parameters  $\theta_i$  using ADAM
6: end for
7: return  $\Theta, \mathbf{R}$ 
```

---

using information about the minimum and maximum physically feasible value of each input dimension, we scale the unit cube to span the whole state space. During research, we tested other methods like random sampling and Latin Hypercube based methods, which turned out to leave "holes" in training data set, meaning non-constant predictive performance over the entire data set. Sobol sequences, meanwhile, span the entire input space more evenly. Sobol sequences are a space filling desing akin to Latin Hypercubes, providing optimality (observed experimentally) in generation of training data. We further evaluate the computational model  $F(x)$  at each training point, obtaining states  $\mathbf{X} \in \mathbb{R}^{N \times m}$  and model outputs  $\mathbf{Y} \in \mathbb{R}^{N \times n}$ .

### 3 The Orbiting Carbon Observatory 2

In this section, we describe OCO-2 and the related measurements, physics model, state vector, and retrieval algorithm. Further information on these topics can be found in e.g. Connor et al. (2008), O'Dell et al. (2012), Crisp et al. (2012), O'Dell et al. (2018), and in the Algorithm Theoretical Basis document (ATBD) Crisp et al. (2021).

#### 3.1 The OCO-2 Instrument

OCO-2 is a NASA operated satellite mission dedicated to providing data products of global atmospheric carbon dioxide concentrations (Crisp et al., 2004). The satellite is pointed towards Earth as it measures solar light reflected by Earth's surface and atmosphere, recorded as radiances. The OCO-2 instrument itself is composed of three spectrometers that measure light reflected from Earth's surface in the infrared part of the spectrum in three separate wavelength bands. These bands are centered around 0.765, 1.61 and 2.06  $\mu\text{m}$  and are called the  $\text{O}_2$  A-band ( $\text{O}_2$ ), the Weak  $\text{CO}_2$  band (WCO<sub>2</sub>) and the Strong  $\text{CO}_2$  band (SCO<sub>2</sub>), respectively. Each observation consists of 1016 radiances on separate wavelengths from each band (for more information, see e.g. Crisp et al. (2017), Rosenberg et al. (2017)). These measurements are then used to infer a state vector containing information on atmospheric properties like  $\text{CO}_2$  concentration on 20 pressure levels, surface pressure, temperature and aerosol optical depth (AOD). The state vector also includes surface properties like albedo, and solar induced chlorophyll fluorescence (SIF). The primary scalar quantity of interest is the column-averaged  $\text{CO}_2$  concentration ( $\text{XCO}_2$ ).



### 3.2 Atmospheric Radiative Transfer

A key part to inferring XCO<sub>2</sub> from observed radiances is construction of a computational atmospheric radiative transfer model which describes how solar radiation is propagated, reflected and scattered by Earth’s surface and atmosphere. Together with an instrument model, this computer code is known as the Full Physics (FP) model, referred to in this work as

$$\mathbf{y} = F(\mathbf{x}, \mathbf{b}), \quad (8)$$

where  $\mathbf{y}$  is output of the FP model, a wavelength-by-wavelength radiance,  $\mathbf{x}$  is a state vector containing atmospheric and surface information, and  $\mathbf{b}$  are model parameters held fixed during data processing. A thorough description of the FP model is given in the ATBD (Crisp et al., 2021). To motivate our emulation approach, we will here describe parts of the forward model physics, which is not intended to be a full description of the included physics. Rather, we leverage this information to better design our emulator.

Part of the radiance comes from absorption of radiation by atmospheric molecules, given by

$$I(\lambda) = f_0(\lambda) \cos(\tau_0) \cdot R(\lambda, \theta, \theta_0, \varphi - \varphi_0) \exp(-g(\lambda)) \quad (9)$$

where  $\lambda$  is wavelength, s.t. the  $j$ th wavelength corresponds to the  $j$ th entry of radiance  $y$ ,  $f_0(\lambda)$  is the solar flux at the top of the atmosphere,  $R(\lambda, \theta, \theta_0, \varphi - \varphi_0)$  is the reflectance of the surface,  $g(\lambda)$  is a integral over radiation path length that sums over for all modeled absorbers,  $\theta$  and  $\varphi$  are the observation zenith and azimuth angles, and  $\theta_0$  and  $\varphi_0$  are the corresponding solar zenith and azimuth angles. Observation and solar angles have a significant effect on the observed and modeled radiances, which will be important later in this work.

After calculating the absorption with equation (9), equations further describing atmospheric scattering are employed to solve for *atmospheric radiative transfer* (RT), which describes the total effect of atmosphere and surface on the scattered photons. The FP framework further includes an instrument model, which describes the effects of the observing system to the *top of the atmosphere radiances*. These effects include instrument doppler shift, spectral dispersion and convolution with the instrument line shape (ILS) function, reducing the resolution from the finer RT grid to the coarser observational grid. On an abstracted level, this corresponds mathematically to

$$I_{OBS}(\lambda) = C_1(\lambda) \int_{-\infty}^{+\infty} RT(\lambda') ILS(\lambda, \lambda') d\lambda' + C_2(\lambda), \quad (10)$$

where  $C_1(\lambda)$  and  $C_2(\lambda)$  denote the instrument effects other than convolution that can be expressed as multiplication and addition. Generally speaking, the instrument effects depend on different physical properties that can vary between detector arrays, while the RT portion of the forward model is constant within the instrument. This observation motivates us to focus on emulating the outputs of the RT, referred to as *monochromatic radiances*, after which instrument functions can be applied appropriately after the fact. Looking forward to operational integration of our emulator, this will reduce the complexity of the emulated system and arguably make our task easier.

### 3.3 OCO-2 State Vector

The state vector elements comprising  $\mathbf{x}$  for the FP model are summarized in Table 1. Notably, we have divided the table in two parts. The upper half lists the previously-mentioned atmospheric and surface state vector elements that affect the RT part only, and the rest having to do with the instrument effects are in the lower half. This collection includes scaling factors for empirical orthogonal functions (EOFs) that capture unmodeled offsets in the observed radiances O'Dell et al. (2018).

State vector element	# elements	O2	WCO2	SCO2
CO2 concentration profile	20		✓	✓
H2O Scaling factor	1	✓	✓	✓
Surface Pressure (Pascals)	1	✓	✓	✓
Temperature Offset (Kelvin)	1	✓	✓	✓
Aerosol height, width and AOD	12	✓	✓	✓
O2 band albedo	2	✓		
WCO2 band albedo	2		✓	
SCO2 band albedo	2			✓
O2 band dispersion	2	✓		
WCO2 band dispersion	2		✓	
SCO2 band dispersion	2			✓
O2 band EOF scaling	3	✓		
WCO2 band EOF scaling	3		✓	
SCO2 band EOF scaling	3			✓
SIF parameters	2	✓		

**Table 1.** Elements of the OCO-2 state vector by functional group. The second column indicates the total elements per group. The check marks in the remaining columns indicate which wavelength bands are sensitive to changes on each variable.

In addition to state vector elements, the FP model is parametrized by a set of parameters that are held fixed based on auxiliary information, such as laboratory measurements or meteorological datasets. These parameters include instrument calibration details, spectroscopy properties for absorbing gases, land elevation, and aerosol microphysical parameters. These aerosol parameters arise from the selection of two dominant aerosol types as a function of space and time. All aerosol types have different optical properties. This choice is determined a priori by global maps based on meteorological knowledge and measurements (see Figure 1). The possible dominant aerosol types are dust (DU), sulphate (SO), sea salt (SS), organic carbon (OC), and black carbon (BC). While constructing the emulator, we will consider datasets with a fixed pair of dominant aerosol species in order to decouple their physical effects from the rest of state vector. Separate emulators can then be constructed for each pair

of aerosol species, and a selection of which one to use can be done by matching the measurement location with the appropriate types.

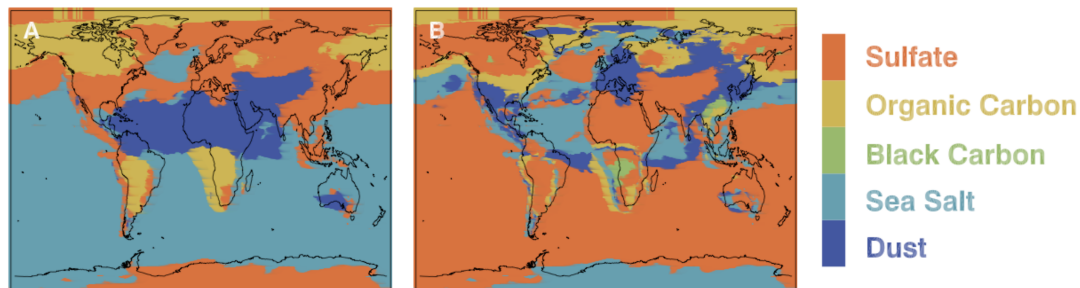


**Figure 1.** Example global map of A) primary and B) secondary aerosol types used in the OCO-2 FP model. Different aerosol types imply different physics, which needs to be taken into account when building a forward model emulator. Image taken from (Boesch et al., 2015)

### 3.4 ReFRACtor

285 This work develops a proof-of-concept version of OCO-2 forward model emulator for a simulated case. For this reason and ease  
of access, we implement our simulations using The Reusable Framework for Atmospheric Composition (ReFRACtor, McDuffie  
et al. (2018)). ReFRACtor is an extensible multi-instrument atmospheric composition retrieval framework that supports and  
facilitates combined use of radiance measurements from different instruments in the ultraviolet, visible, near-infrared and  
thermal-infrared. It has been open source since 2014 when it was first developed as the Level-2 processing code for OCO-2.  
290 Since 2017 the development team has worked to create a more general framework that supports more instruments and spectral  
regions. This framework has been developed to provide the broader Earth science community a freely licensed software package  
that uses robust software engineering practices with well tested, community accepted algorithms and techniques. ReFRACtor  
is geared not only for the creation of end-to-end production science data systems, but also towards scientists who need a  
software package to help investigate specific Earth science atmospheric composition questions. Although ReFRACtor includes  
295 an implementation of a version of the OCO-2 production algorithm, the two have drifted since the initial inter-comparison  
comparison work was done. At that time it was validated against the B9.2.00 version of the software. For the most part mainly  
bug fixes have been kept in sync between the two versions. Additionally the core radiative transfer algorithms are the same,  
which justifies the use of ReFRACtor for constructing our emulator at this stage. Some minor additional algorithmic features  
made their way into the ReFRACtor version of OCO-2 from the production version. For the most part the major discrepancy  
300 will be due to changes to configuration values not implemented in ReFRACtor. These include values such as a priori and  
covariance version, EOF datasets, ABSCO versions and the solar model.

### 3.5 Retrieval Algorithm

Inferring XCO<sub>2</sub> from measured radiances is an ill-posed inverse problem, which is referred to as performing a retrieval. The relationship between measurement and state is first modeled as

$$305 \quad \mathbf{y} = F(\mathbf{x}) + \varepsilon, \quad (11)$$

where data  $\mathbf{y} \in \mathbb{R}^n$  is a radiance vector, unknown  $\mathbf{x} \in \mathbb{R}^m$  is the state vector,  $F: \mathbb{R}^m \rightarrow \mathbb{R}^n$  is the OCO-2 FP model and  $\varepsilon \in \mathbb{R}^n$  is the measurement uncertainty. For completeness, we summarize the operational retrieval algorithm used in OCO-2 processing. The retrieval proceeds with solving the inverse problem by using Bayesian formulation, in which the additive error  $\varepsilon$  and prior for  $\mathbf{x}$  are assumed to be Gaussian, such that

$$310 \quad \varepsilon \sim \mathcal{N}(0, \mathbf{S}_\varepsilon), \quad \mathbf{x} \sim \mathcal{N}(\mathbf{x}_a, \mathbf{S}_a). \quad (12)$$

The measurement error covariance matrix  $\mathbf{S}_\varepsilon$  is assumed to be diagonal, with elements for each wavelength  $j$  given by

$$\sigma_j^2 = k_1 y_j + k_2, \quad (13)$$

where  $k_1$  and  $k_2$  are calibration parameters adjusted by the instrument calibration team. The a priori covariance is taken to be diagonal for non-CO<sub>2</sub> parameters, and the CO<sub>2</sub> profile is assumed to have a correlation structure shown in in Figure 2, which

315 promotes continuous concentration profiles and limits the variability higher up in the atmosphere.

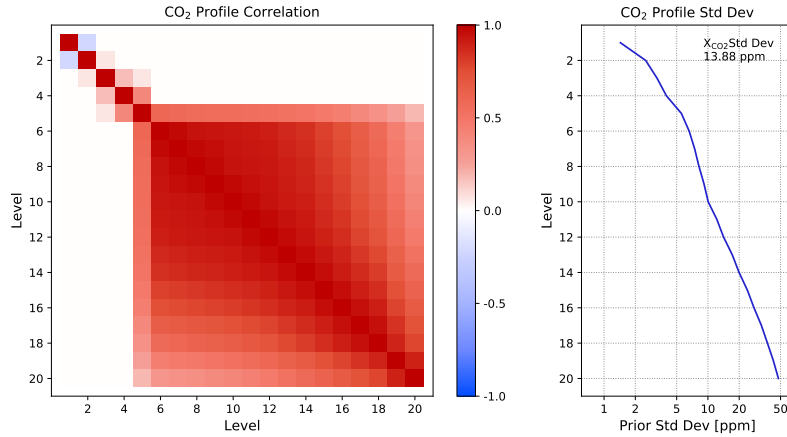


**Figure 2.** The a priori correlation matrix and standard deviation used for the CO<sub>2</sub> vertical profile in the OCO-2 retrieval. Vertical levels are ordered from the top of the atmosphere (Level 1) to the surface (Level 20).

The retrieval is operationally carried out using iterative gradient-based methods to solve for the maximum a posteriori estimate, which is equivalent to minimizing the cost function

$$\hat{\mathbf{x}} = \underset{\mathbf{x}}{\operatorname{argmin}} (\mathbf{y} - F(\mathbf{x}))^T \mathbf{S}_\varepsilon^{-1} (\mathbf{y} - F(\mathbf{x})) + (\mathbf{x} - \mathbf{x}_a) \mathbf{S}_a^{-1} (\mathbf{x} - \mathbf{x}_a) \quad (14)$$

This optimization problem is solved using the Levenberg-Marquardt algorithm, in which at iteration  $i$  the state is updated  
 320 according to

$$((1 + \gamma)\mathbf{S}_a^{-1} + \mathbf{K}_i^T \mathbf{S}_\varepsilon^{-1} \mathbf{K}_i) d\mathbf{x}_{i+1} = [\mathbf{K}_i^T \mathbf{S}_\varepsilon^{-1} (\mathbf{y} - F(\mathbf{x}_i)) + \mathbf{S}_a^{-1} (\mathbf{x}_a - \mathbf{x}_i)] \quad (15)$$

where  $\gamma$  is a damping parameter and  $\mathbf{K}_i$  is the Jacobian of  $F(\mathbf{x})$  at iteration  $i$ . After each iteration, before updating the state, the effect of forward model non-linearity is assessed by computing the quantity

$$R = \frac{c_i - c_{i+1}}{c_i - c_{FC}}, \quad (16)$$

325 where  $c_i$  is the value of the cost function (14) at iteration  $i$ ,  $c_{i+1}$  similarly at iteration  $i + 1$ , and  $c_{FC}$  is the cost function value assuming that  $F(\mathbf{x}_i + d\mathbf{x}_{i+1}) = F(\mathbf{x}_i) + \mathbf{K}_i d\mathbf{x}_{i+1}$ ; that is, a linear update. Based on the value of  $R$ , one of the following is executed:

- $R \leq 0.0001$ :  $\gamma$  is increased by a factor of 10. State is not updated.
- $0.0001 < R < 0.25$ :  $\gamma$  is increased by a factor of 10,  $\mathbf{x}_{i+1} = \mathbf{x}_i + d\mathbf{x}_{i+1}$
- 330 –  $0.25 < R < 0.75$ :  $\mathbf{x}_{i+1} = \mathbf{x}_i + d\mathbf{x}_{i+1}$
- $R > 0.75$ :  $\gamma$  is decreased by a factor of 2,  $\mathbf{x}_{i+1} = \mathbf{x}_i + d\mathbf{x}_{i+1}$

After each non-divergent step, convergence is assessed by computing the error variance derivative (see Crisp et al. (2021) for details). The operational retrieval further provides an estimate for the posterior covariance as a Laplace approximation

$$\hat{\mathbf{S}} = (\mathbf{K}^T \mathbf{S}_\varepsilon^{-1} \mathbf{K} + \mathbf{S}_a^{-1})^{-1}, \quad (17)$$

335 together with the so-called *Averaging Kernel*

$$\mathbf{A} = (\mathbf{S}_a^{-1} + \mathbf{K}^T \mathbf{S}_\varepsilon^{-1} \mathbf{K})^{-1} \mathbf{K}^T \mathbf{S}_\varepsilon^{-1} \mathbf{K} \quad (18)$$

which can be interpreted as the sensitivity of the retrieved state  $\hat{\mathbf{x}}$  to the true atmospheric state  $\mathbf{x}$ . These quantities are important for downstream users of OCO data products, which highlights the value of producing closed-form Jacobians during data processing.

## 340 4 Forward Model Emulation

In this section, we will describe the practical implementation of our method laid out in Section 2 applied to the OCO-2 retrieval problem in Section 3. This includes data transformations and dimension reduction, training data generation, convergence of the optimizer in kernel parameter learning, and assessment of forward model output quality. We stress that in order to be

implemented in an operational retrieval algorithm, the emulator is required to perform with superior accuracy. We ensure  
 345 accurate performance by making sure that the error in predicted radiances, compared to FP outputs, is less than the radiance  
 measurement error standard deviation. This way, any systematic errors in emulation will be masked by measurement noise,  
 and retrieval performance using emulation will closely resemble that of using FP.

#### 4.1 Data transformations

As GPs tend to perform worse with increasing input dimension, and because the standard GP formulation is developed for one  
 350 dimensional outputs, we will need to reduce the dimension of both the atmospheric state and the radiance. For the atmospheric  
 state  $\mathbf{x}$ , we leverage the fact that OCO-2 measurements are made at 3 separate wavelength bands, which leads to the state vector  
 having band-specific elements which can be ignored when dealing with other bands. This partition has been summarized in  
 Table 1. Earlier work by Ma et al. (2019) considered cross-band correlations while emulating OCO-2 radiances, but the authors  
 finally showed that the bands are distant enough from one another in wavelength space that they can be treated independently.  
 355 With this insight, we proceed by constructing separate GPs for each band and using only the sensitive dimensions of  $\mathbf{x}$  as  
 inputs. We further notice that the 20 element CO<sub>2</sub> profile is continuous and can be expressed as loadings obtained using  
 principal component analysis (PCA). The most straightforward way to do this is by truncated singular value decomposition  
 (SVD) of the empirical covariance matrix of state vectors (Tukiainen et al., 2016). To accomplish this, we use a simulation  
 distribution derived by Braverman et al. (2021) for one selected set of realistic geophysical conditions as a basis for our  
 360 experiments and perform SVD on the covariance matrix of this distribution. Analysis of singular value decay suggests that the  
 CO<sub>2</sub> profile can be represented with just 4 principal components, which we collect to a matrix  $\mathbf{P}_x$  as the 4 leading singular  
 vectors. We then project the CO<sub>2</sub> profile to principal component space, and further standardize the states by using the mean  
 and variance of the simulation distribution, leading to

$$\tilde{\mathbf{x}} = \frac{1}{\sigma_x} (\text{diag}(\mathbf{P}_x^T, \mathbb{I}_c)(\mathbf{x} - [\boldsymbol{\mu}_p, \mathbf{0}_c]) - \boldsymbol{\mu}_x), \quad (19)$$

365 where  $\boldsymbol{\mu}_p$  is the CO<sub>2</sub> profile mean,  $\boldsymbol{\mu}_x$  and  $\sigma_x$  are the state mean and state standard deviation,  $\text{diag}(A, B)$  denotes a block  
 diagonal matrix with blocks  $A$  and  $B$ ,  $\mathbb{I}_c$  is a  $c = m - 16$  dimensional identity matrix (as the profile is represented by 4  
 dimensions instead of original 20), and  $[\boldsymbol{\mu}_p, \mathbf{0}_c]$  is a stacked vector of CO<sub>2</sub> profile mean and a  $c$  dimensional zero vector.

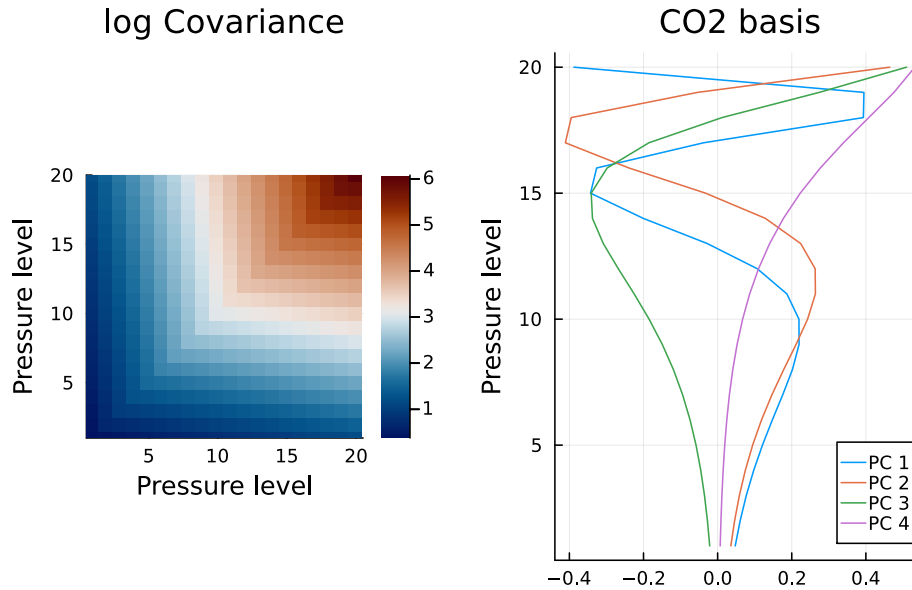


**Figure 3.** Left: the CO<sub>2</sub> profile covariance matrix of the simulation distribution used in this work. Right: 4 leading singular vectors from the SVD of the covariance matrix.

Next, we generate training data using a Sobol sequence (see Section 2.4). For this study, we can omit dispersion, EOF and SIF parts of the state vector (see Table 1) and fix them to the prior mean. This follows from the discussion in Section 3 focusing on monochromatic radiances. Omitting dispersion simplifies computations as the wavelength grid would otherwise shift, making SVD for radiance dimension reduction hard. Ma et al. (2019) solved this problem by employing Functional Principal Component Analysis, while we can proceed with ordinary SVD. The Empirical Orthogonal Functions (EOFs) are included in the operational retrieval to reduce fit residuals and therefore make convergence analysis easier. These has no direct impact on our study and can be safely omitted. Furthermore, the SIF parameters are fit on the O<sub>2</sub> band only as part of the instrument effects, and we do not include them in the emulation for this reason. As is evident from equation (9), the measurement geometry has a significant impact on the output of the FP model. For this reason we include three extra parameters,  $\theta$ ,  $\theta_0$ , and  $\varphi - \varphi_0$  to our training data vector. Sufficient and realistic limits to these parameters are obtained from the simulation distribution of Braverman et al. (2021) by considering a  $4\sigma$  interval around the mean values. In all, we now have  $m = 4 + 21 + 3 = 28$  for input space, coming from profile PCs, other included state vector elements and geometry. We create a Sobol sequence of 20 000 points for training, and scale all dimensions of the hypercube to  $[-4, 4]$ , corresponding to 4 standard deviations in the normalized  $\tilde{x}$  basis. We further obtain the training data set in original space by reversing the transformation (19).

Training data  $\mathbf{Y}$  (radiances) are obtained by evaluating the FP model on each  $\mathbf{x}$  from the scaled Sobol sequence. For this work, we choose a single realistic land nadir measurement to represent physical parameters not included in state vector  $\mathbf{x}$ . We perturb sampling geometry to reflect relevant solar and instrument angles. For a real-world application this approach can be

extended to include different scenes and other location-dependent parameters. To obtain the labels  $z$ , we similarly perform truncated SVD on the radiances  $Y$  separately on each wavelength band  $B \in [O2, WCO2, SCO2]$ , and collect the leading  $n_B$  singular vectors in matrices  $P_B$ . The four leading singular vectors for each band are included in Figure 4 for presenting the kinds of features the most significant principal components, or basis vectors, encode. While this decomposition could hold additional information on physical processes behind the radiative transfer model, we don't pursue such analysis further in this work. With additional standardization of the variables, we obtain the following transformations for each wavelength band  $B$ :

$$\tilde{z}_B = \frac{1}{\sigma_z} (P_B^T (y_B - \mu_B) - \mu_z) \quad (20)$$

where  $\mu_B$  is the radiance mean, and  $\mu_z, \sigma_z$  are the principal component mean and standard deviation for band  $B$ .

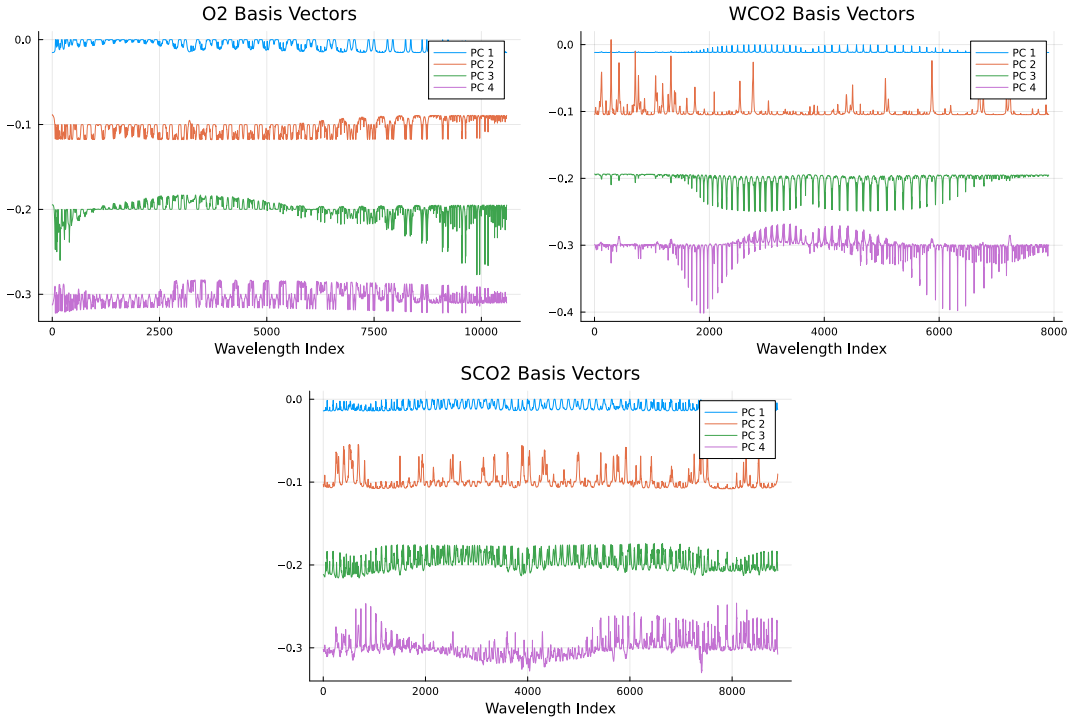


**Figure 4.** Leading 4 basis vectors obtained from the SVD (principal components, PC) for radiances  $y$  for each band: O2, Weak CO2 (WCO2) and Strong CO2 (SCO2). Basis vectors 2-4 are offset for illustration purposes.

The quality of this approximation is assessed by plotting the reconstruction  $P_B P_B^T (y_B - \mu_B) + \mu_B$  over a heldout dataset not used in computing the SVD. We illustrate in the upper panel of figure 5 the distribution of relative reconstruction error from this dataset. We have further applied the instrument function to each residual and further divided them by the measurement error standard deviation given by equation (13). This metric is justified by the rationale that if the reconstruction error is less or comparable to measurement error on the radiances, no significant amount of information is lost.



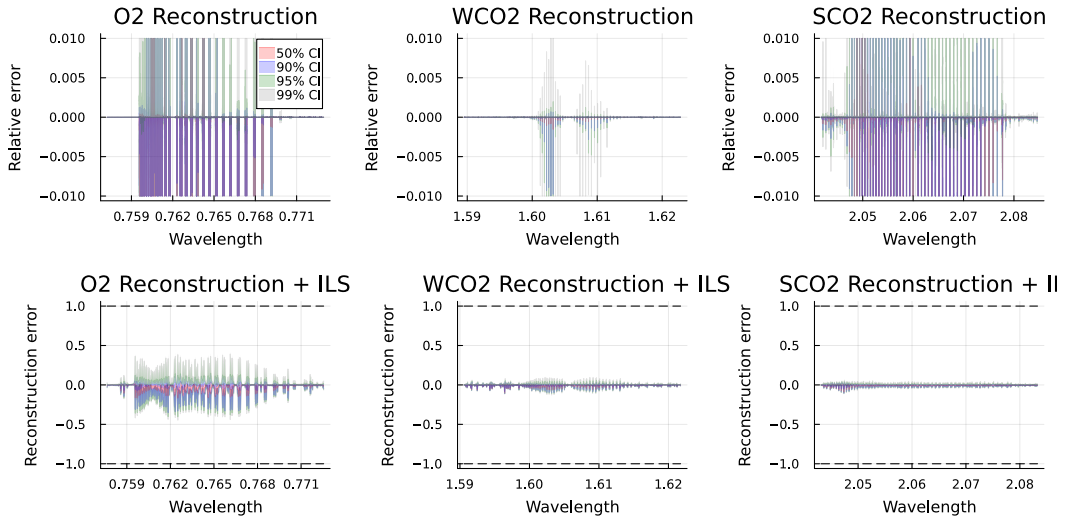


**Figure 5.** Upper row: distribution of relative reconstruction error for monochromatic radiances on the  $O_2$ ,  $WCO_2$  and  $SCO_2$  bands. Lower row: distribution of reconstruction error for all bands after applying the instrument function and dividing by measurement error standard deviation. Shading represents 50% (red), 90% (blue), 95% (green) and 99% (gray) confidence intervals.

The final emulator  $g(\mathbf{x})$  can now be summarized in Figure 6, where  $GP_i(\tilde{\mathbf{x}}_B)$  is the GP prediction given by equation (1) and the indices  $i, j, k$  run through the number of principal components included in a given band. The effect of this choice will be examined further later in this work. The state is first normalized according to 19 for each band  $B$ , after which the GP predicted principal component loadings are assembled back to radiances using relation 20. When evaluating the emulator, each index is independent and can then be computed in parallel.

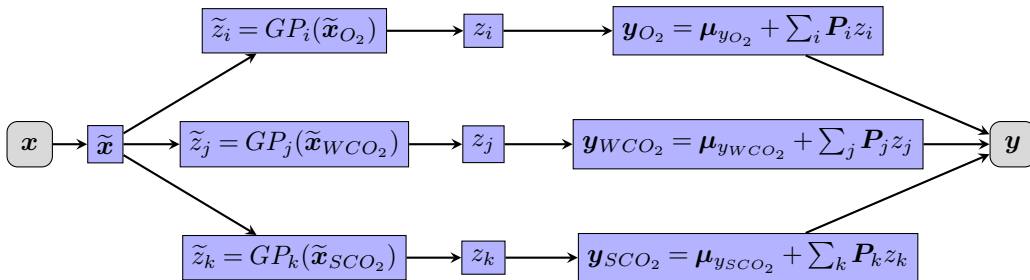


**Figure 6.** Diagram showing the step-by-step process of emulator evaluation. Transformation  $\tilde{\mathbf{x}}$  refers to normalization in 19, similarly  $\tilde{z}$  denotes the scaling given in 20.  $GP(\tilde{\mathbf{x}})$  denotes the GP prediction given by 1 of labels  $z$ , which are assembled back to radiances based on 20 for each band and each principal component  $i, j, k$  therein.

## 4.2 Training

405 Having obtained training data  $\widetilde{\mathbf{X}}, \mathbf{z}$ , we can now proceed to optimize the kernel parameters as described in section 2.3. We prescribe an individual GP per output parameter  $z_i$ . We have  $N = 20000$  for training data size, and we set  $M = 100$  for mini-batch size,  $p = 5$  for the number of prediction points per mini-batch, and run the ADAM optimizer for 5000 iterations with a small learning rate; in our case 0.02. We initialize all other parameters at 1, except for linear component weight at 0 and the nugget at 1e-6. For  $\widetilde{\mathbf{x}}$ . As outlined in Section 3.3, we further reduce the dimension of the input space by selecting only the  
410 indices that a given wavelength band is sensitive to, given by Table 1.

For testing the performance of the algorithm, we draw a random sample  $\mathbf{X}^{\text{test}}$  from the same simulation distribution from (Braverman et al., 2021) as independent test data, which is then used to evaluate the FP model to create radiances  $\mathbf{Y}^{\text{test}}$ . For test data, we fix dispersion, EOFs and SIF at prior values as before. Example behavior of the loss function together with evolution of the kernel parameter values and true vs predicted  $z$  values for is shown in Figure 7. We see that during training, the loss  
415 function values converge to a small value close to 0. The fluctuations of loss function values are due to ADAM optimizer effectively being a stochastic gradient descent method: each mini-batch is sampled randomly, which causes consequent steps possibly resulting in higher values, while the running average still always decreases. We can also see the evolution of different kernel parameters: the weight of the linear component, for example, was initially set very close to 0. During training, the algorithm correctly identifies the significance of the linear term, and the relative importance of this term overtakes the nugget  
420 (corresponding to random noise). Resulting predictions of principal component loadings can be seen to land very tightly on the 1-to-1 line, indicating good performance over the whole test data. The distribution of true vs predicted  $z$  values for each component on each wavelength band is further illustrated in Figure 8. We conclude that the predicted values correspond the true values most of the time. Some principal components show larger spread on prediction errors, e.g. O2 PC 9 or WCO2 PC 9. These principal components can be redundant and not contain meaningful information about the radiance, since the total  
425 predictive performance still remains very accurate,

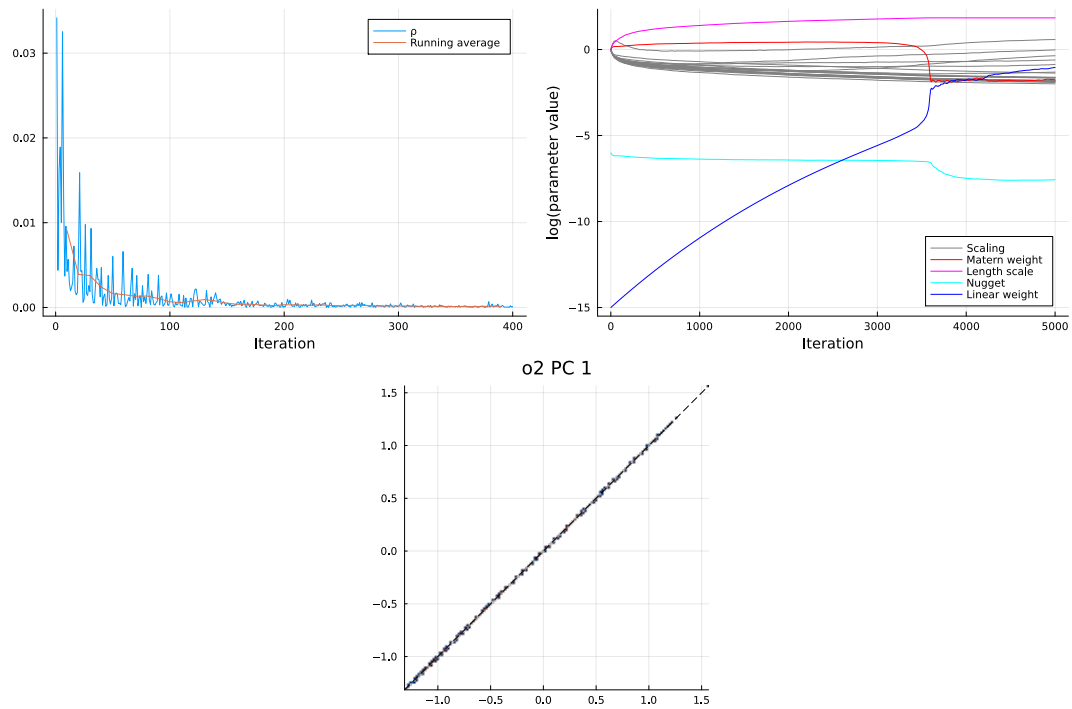


**Figure 7.** Example training performance for the first principal component of the O<sub>2</sub> band. Upper left: loss function values for the first 400 iterations of parameter learning. Blue line depicts the cost function value per iteration. Red line depicts a cumulative running average of the cost function. Upper right: evolution of the kernel parameters as function of iteration. Lower center: true vs predicted  $z$  values over a withheld test set for the first component of O<sub>2</sub> band.

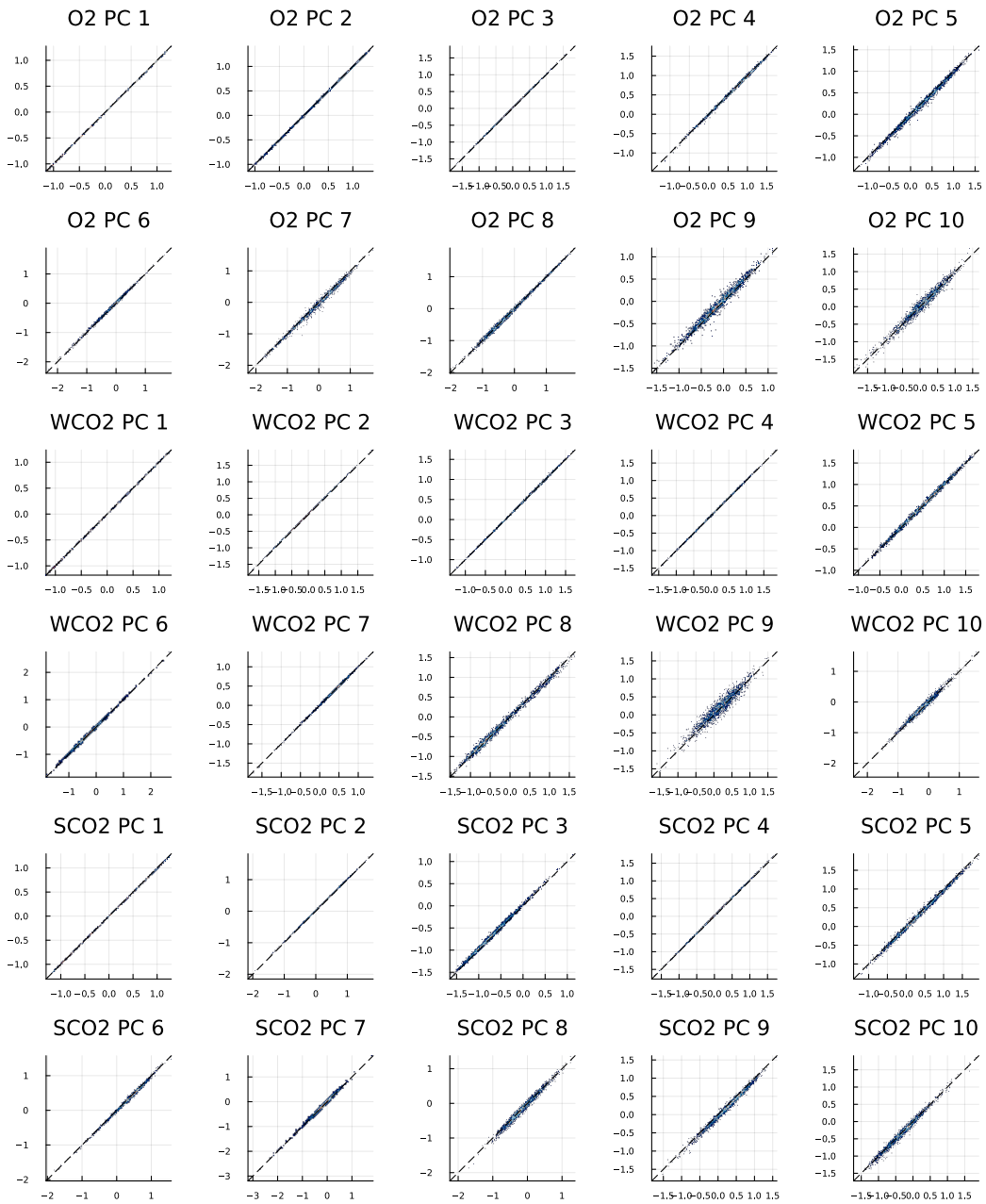


**Figure 8.** True versus predicted values for 10 radiance principal components on each wavelength band.

### 4.3 Predictive performance

Finally, we assemble the predicted  $z$  values back to radiances and compute the relative differences with the test data, shown in the upper panel of figure 9. On the lower panels, as before, we apply the instrument function to these residuals and divide by

430 measurement error standard deviation to underline that desired performance would be to make less prediction error than is the measurement error.

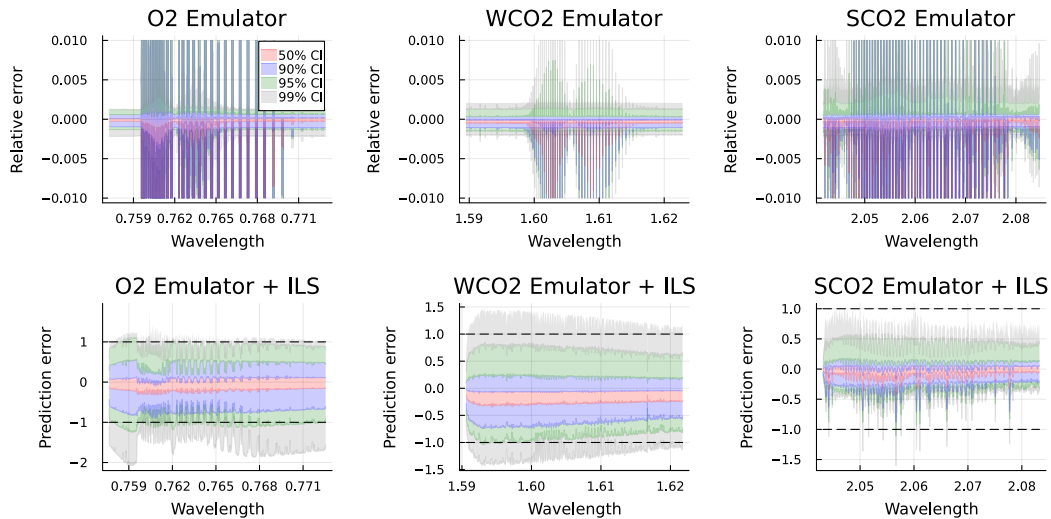


**Figure 9.** Upper row: distribution of relative prediction error for monochromatic radiances on the O<sub>2</sub>, WCO<sub>2</sub> and SCO<sub>2</sub> bands. Lower row: distribution of prediction error for all bands after applying the instrument function and dividing by measurement error standard deviation. Shading represents 50% (red), 90% (blue), 95% (green) and 99% (gray) confidence intervals.

435 After constructing the emulator obtaining radiances as outputs, we can further apply equation (3) to compute the Jacobians  $\frac{d}{d\tilde{\mathbf{x}}}$   $\mathbf{z}$ . We can then reverse the normalizing transformations on both  $\tilde{\mathbf{x}}$  and  $\mathbf{y}$  and further apply the instrument functions to our Jacobians to get back to the operational observation units. The Jacobians obtained by evaluating both FP and emulator on an example state vector together with the resulting profile averaging kernels are shown in Figure 10. Accurate averaging kernels are important for downstream usage of the retrieved XCO<sub>2</sub>, as it is used e.g. in flux inversion models to obtain the vertical sensitivity of XCO<sub>2</sub> to modeled atmospheric CO<sub>2</sub> profiles. We note that we have normalized the Jacobians and averaging kernels by maximum values of each row in the matrix for visual clarity. Although not perfectly similar, we conclude that these two outputs share significant similarity. The main difference on the averaging kernels mainly results from the choices on modeling concentration profiles by principal component loadings.

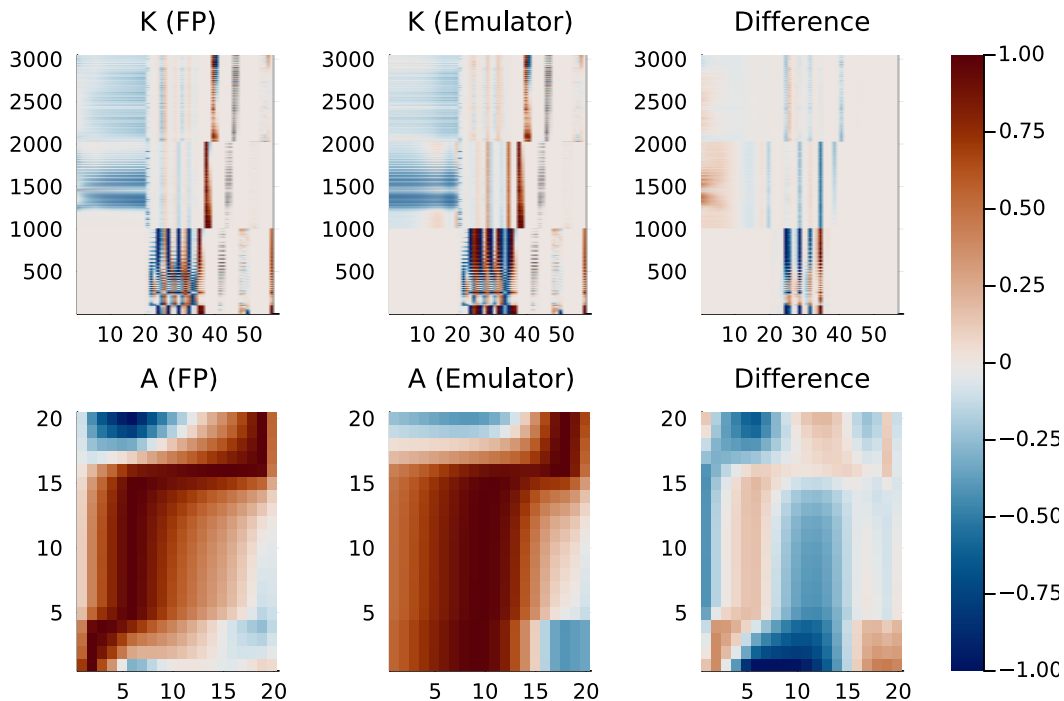


**Figure 10.** Normalized Jacobians  $K$  and profile averaging kernels  $A$  from both the FP and emulator, together with the corresponding differences.

440 As noted in previous work by Ma et al. (2019), an emulator provides substantial appeal in terms of computational efficiency. For the current work, the average computational times for model evaluation and Jacobians are summarized in Table 2 on a 2023 MacBook Pro. It is worth mentioning that ReFRACtor computes Jacobians via automatic differentiation, while our emulator does this analytically. Three cases are contrasted: the standard ReFRACtor FP evaluation, the emulator for monochromatic radiances plus ILS, and the emulator alone.

**Table 2.** Evaluation times of radiative transfer (RT) model and related Jacobian, comparing the ReFRACtor implementation, monochromatic emulator with instrument line shape (ILS) and other spectral corrections, and monochromatic emulator only.

	RT [s]	RT + Jacobian [s]
ReFRACtor	33.45	55.26
Emulator + ILS	2.06	2.17
Emulator	0.05	0.19

#### 445 4.4 Faster Research Version

In recent years, the uncertainty quantification and statistics community has benefited enormously by utilizing the surrogate model by (Hobbs et al., 2017) to explore the OCO-2 retrieval in numerous applications (Brynjarsdóttir et al. (2018), (Lam-

minpää et al., 2019), Nguyen and Hobbs (2020), Hobbs et al. (2021), Patil et al. (2022)). We remark that for similar purposes, our emulator can be used as an even faster surrogate. As we see from Table 2, the majority of the computational cost for the emulator comes from the instrument effects which is part of the ReFRACtor software. If one is not interested in including the effects of dispersion, SIF, and EOF's during the retrieval, we notice from equation (10) that instrument corrections to RT amount to multiplication, addition, and convolution, which is associative wrt. multiplication. We can then write the emulator as

$$g(\mathbf{x}) = ILS\left(\widehat{\mathbf{P}}\eta(\mathbf{x})\right) = ILS\left(\widehat{\mathbf{P}}\right)\eta(\mathbf{x}), \quad (21)$$

where  $g(\mathbf{x})$  is the overall emulator,  $ILS()$  is a function applying the instrument corrections from equation (10),  $\widehat{\mathbf{P}}$  is a projection matrix consisting of radiance basis functions that corresponds to transforming predicted labels  $\mathbf{z}$  back to radiances  $\mathbf{y}$  following the last step in figure 6, and  $\eta(\mathbf{x})$  is the emulator predicting labels  $\mathbf{z}$  from inputs  $\mathbf{x}$ . Done this way, we can evaluate the instrument corrections on the basis vectors once, after which OE or MCMC can proceed an order of magnitude faster (according to table 2).

## 5 Retrievals using the Emulator

We are now ready to compare the performance of the emulator against the FP model when performing simulated retrievals. After obtaining the minimizer  $\widehat{\mathbf{x}}$  and a Laplace approximation of posterior covariance,  $\widehat{\mathbf{S}}$ , the quantity of interest is further given by multiplying the CO<sub>2</sub> profile by the pressure weighting function  $\mathbf{h}$  that puts an appropriate weight for each pressure level, resulting in

$$\text{XCO}_2 = \mathbf{h}^T \widehat{\mathbf{x}}_{1:20}. \quad (22)$$

The reported uncertainty coming with the Quantity of Interest (QoI) is given by

$$\text{XCO}_{2\text{uncert}} = \sqrt{\mathbf{h}^T \widehat{\mathbf{S}}_{1:20,1:20} \mathbf{h}}. \quad (23)$$

We present two test cases for assessing retrieval performance of our emulator. First, we create synthetic observations by evaluating the FP model on our test set of states  $\mathbf{x}$  and adding a realization from the Gaussian noise distribution:

$$\mathbf{y}_{\text{test}} = F(\mathbf{x}, \mathbf{b}) + \varepsilon, \quad (24)$$

where  $\varepsilon \sim N(0, \mathbf{S}_\varepsilon)$ . Second, we follow the methods outlined in Braverman et al. (2021) to further corrupt the simulated measurement by realistic *Model Discrepancy* (MD) adjustment, given by

$$\mathbf{y}_{\text{test}} = F(\mathbf{x}, \mathbf{b}) + \varepsilon + \delta, \quad (25)$$

where  $\delta \sim N(\mu_\delta, \mathbf{S}_\delta)$ . The shape of this adjustment is illustrated in Figure 11. As noted by the authors, model discrepancy as presented here is a statistical representation of forward modeling mismatches so that our simulated measurements would better correspond to real data.

We then perform XCO<sub>2</sub> retrievals both using the Full Physics model  $F(\mathbf{x})$  and the emulator  $g(\mathbf{x})$  following the algorithm laid out in Section 3. Results for retrieved XCO<sub>2</sub> for both cases with and without MD are illustrated in Figure 12. The corresponding XCO<sub>2</sub> uncertainty values are compared in Figure 13. We conclude that using the emulator in place of FP model in retrieval preserves the accuracy and replicates same biases as FP, while having good correlation with each other. On the other hand, the output uncertainty estimates seem to not correspond to each other, and further analysis on this output will be required in future research work.

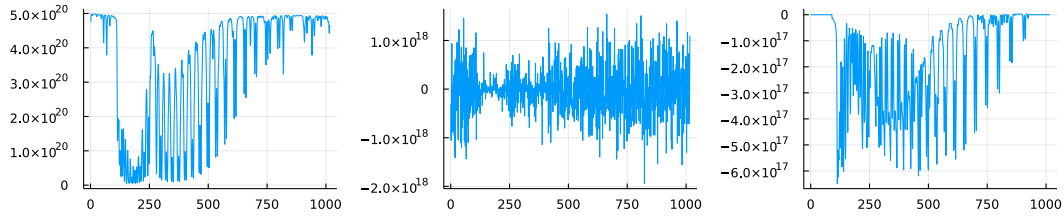


**Figure 11.** Left: example O<sub>2</sub> band radiance. Middle: realization from the noise distribution  $N(0, \mathbf{S}_\varepsilon)$ . Right: realization from the model discrepancy distribution  $N(\mu_\delta, \mathbf{S}_\delta)$ . Units for all panels are  $\text{W m}^{-2} \text{sr}^{-1} \mu\text{m}^{-1}$ , the units of radiance for OCO-2.



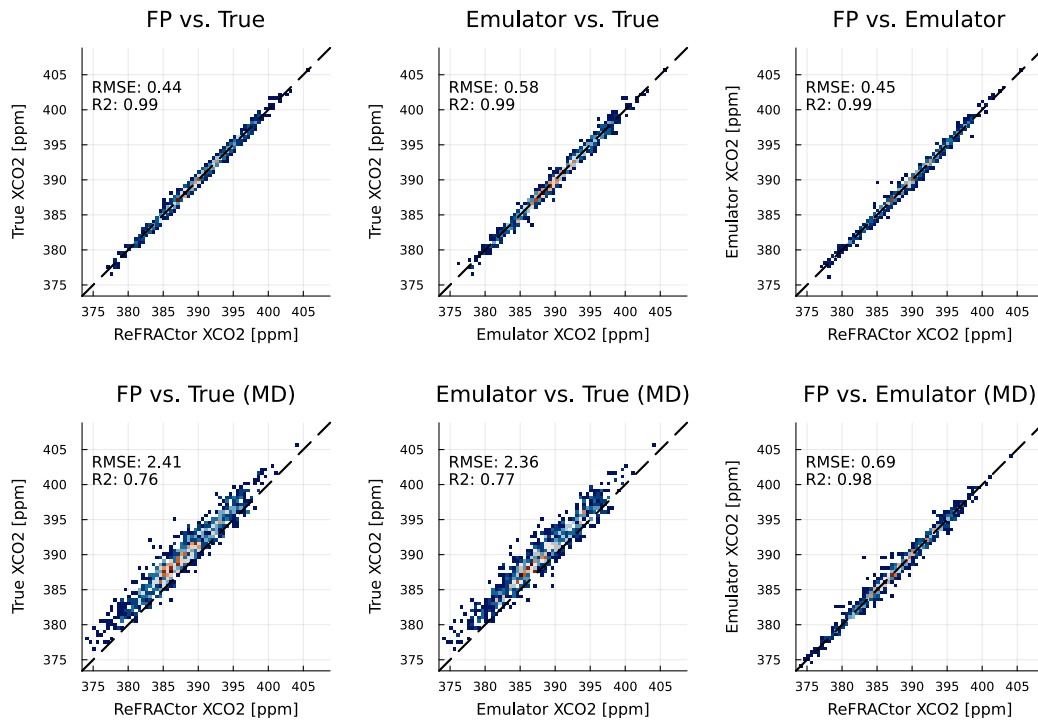


**Figure 12.** Retrieved XCO<sub>2</sub> over heldout dataset using FP and emulator. Upper row: Full Physics (left), Emulator (middle) and comparison of the two (right). Lower row: similarly, but with added model discrepancy in observed data. RMSE (Root mean square error) describes bias of the retrievals while R<sup>2</sup> value is included to assess correlation between quantities of interest.

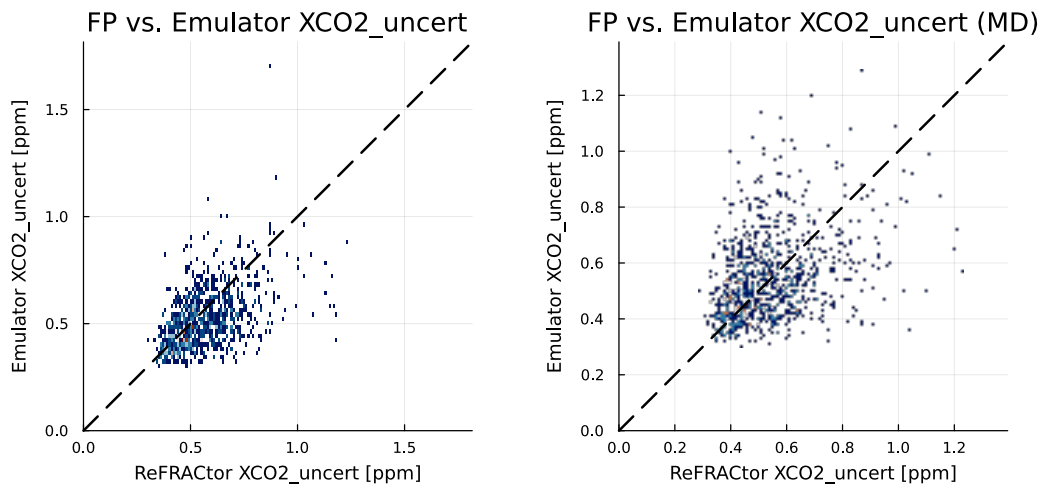


**Figure 13.** Scatter plots of retrieval XCO<sub>2</sub> uncertainty over heldout dataset using FP and emulator. Left: no MD in observations. Right: MD included in observations.

## 5.1 Effect of PCA dimensionality

Previously in this work we have not prescribed a certain number of principal components to use in radiance dimension reduction. Figure 14 illustrates the retrieved XCO<sub>2</sub> root mean square error (RMSE) and mean absolute error (MAE) against the true known value, together with 15 illustrating radiance reconstruction and prediction RMSE and MAE similarly to Figures 5 and 9, all as a function of number of PCs used. We can collectively deduce that using more than 25 principal components per band does not yield any additional performance benefits. We remark that compared to the earlier work by Ma et al. (2019), who argued for 1-3 principal components per band, our results show that many more components are needed for accurate retrievals. This highlights the importance of empirically checking the effect of dimensionality reduction and not relying on rules-of-thumb such as conserving 95% of variability.

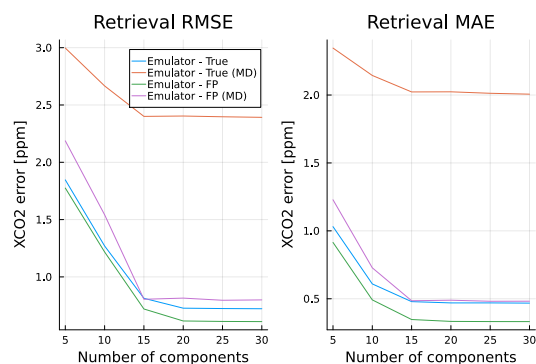


**Figure 14.** RMSE and MAE as a function of number of principal components used per band in radiance dimension reduction for XCO<sub>2</sub> retrievals, both with and without MD, over a heldout test dataset.

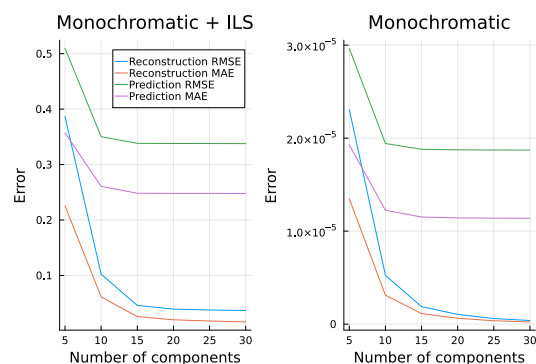


**Figure 15.** RMSE and MAE as a function of number of principal components used per band in radiance dimension reduction reconstructions and predictions, all over a heldout test dataset.

## 5.2 Effect of Aerosol types

To assess the effect of changing the dominant aerosol types on the performance of the retrievals, we repeat the training and retrieval procedure described in this section with two separate pairs of dominant aerosol types. First, we consider dust (DU) and sea salt (SS), and secondly, DU and sulphate (SO). These are among the most common aerosol combinations encountered in the OCO-2 operations. We repeat the retrievals for both cases with additional MD adjustment as before. Results for this experiment are summarized in figure 16. We conclude that the proposed method is robust to changing physical conditions, which indicates fitness for further operational integration.

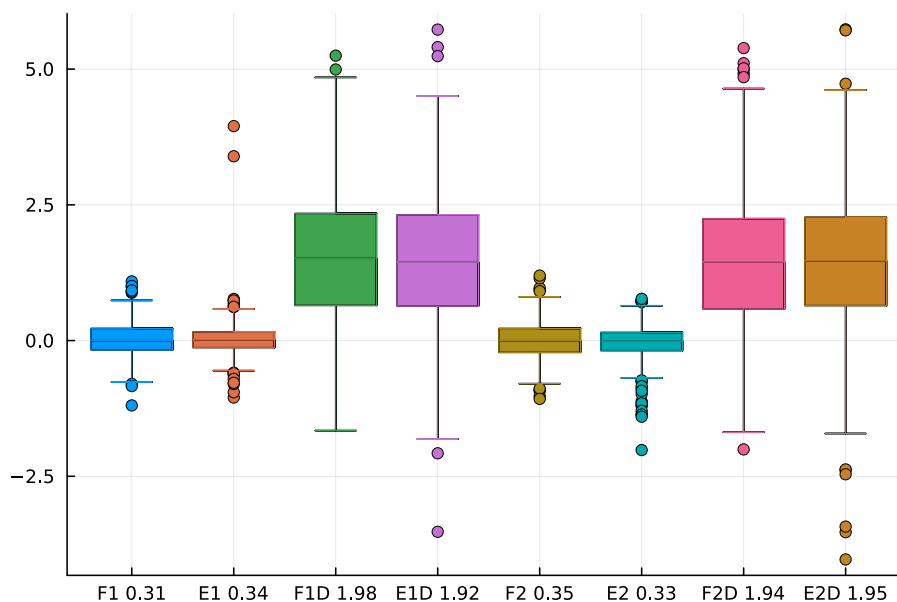


**Figure 16.** Difference in ppm between true and retrieved  $XCO_2$  from simulated measurements with different dominant aerosol species, in ppm. Symbols on x-axis denote the specifics of given experiment: F = Full Physics, E = Emulator. 1 = DU and SS aerosols, 2 = DU and SO aerosols. D = With model discrepancy, followed by a number denoting mean error in ppm.

## 6 Conclusions

In this work, we have constructed and implemented a fast and accurate forward model emulator for the ReFRACtor implementation of the OCO-2 full physics forward model. The emulator produces closed form Jacobians, and as such gives a convenient way of performing  $XCO_2$  retrievals. We have demonstrated the accuracy of these retrievals, and analyzed the effect of PCA dimension, aerosol types and model discrepancy on the retrieval. All these tests indicate robustness and excellent reliability of our method, and offer an encouraging proof of concept for future operational implementation with latest ACOS algorithm and real world OCO-2 data.

This work has significantly advanced the Kernel Flows methodology (Owhadi and Yoo, 2019) by including a cross-validation based training strategy using RMSE cost function and new strategy for mini-batching. With this method, we have achieved a relative error of less than 1% which on its own is a significant improvement from the point of view of operator learning (see for example (Batlle et al., 2023) for comparisons of GP and NN methods on various non-linear problems). Our approach is  
510 computationally fast and, when training data set is properly engineered, performs consistently within the span of training data. Compared with our ability to compute Jacobians in closed form, our approach holds a potential to solve current and future data processing issues in atmospheric remote sensing stemming from computationally intensive forward models.

While Gaussian Process methods offer an attractive means to include uncertainty propagation in emulation pipeline, our tests have shown that the predicted posterior standard deviation given by GPs was not adequate in providing reliable coverage  
515 of true labels after prediction. This is likely due to Kernel Flows method's focus on optimizing the posterior mean prediction without assessing the prediction uncertainty. This could easily be remedied by including a uncertainty tuning penalty in the KF loss function. Another disclaimer comes from evaluations of retrieval uncertainty on XCO<sub>2</sub>: our method was not agreeing with operational OE. This does not mean our estimates were better or worse, and further research is needed in calibrating retrieval uncertainties.

520 A logical next step would be to implement the GP emulator for operational ACOS forward model instead of ReFRACtor, which requires closer collaboration with the OCO algorithm team. After demonstration on OCO-2, our approach is directly applicable for a myriad of other satellite missions. We note that future work will have to deal with training data design that was simplified in this work. Assessing different temporal and spatial variability in forward model parameters together with feasible distributions of state vectors will be key in this design effort. These efforts might benefit from including a cost-benefit  
525 analysis on training a global model usable everywhere versus, for example, re-training the emulator for sufficiently specified spatio-temporal datasets.

*Code and data availability.* Code and data are available at an OSF repository (Lamminpää, 2024). The software depends on ReFRACtor and ReFRACtorUQ git repositories which are freely available as well.

*Author contributions.* O.L.: Project administration, Conceptualization, Methodology, Software, Formal analysis, Data curation, Writing –  
530 Original Draft, Writing - review & editing, Visualization. J.S.: Conceptualization, Methodology, Software, Writing - original draft, Writing - review & editing. J.H.: Project administration, Conceptualization, Methodology, Supervision, Software, Data curation, Writing - review & editing. J.M.: Methodology, Software, Data curation, Writing - original draft. A.B.: Conceptualization, Methodology, Writing - review & editing. H.O.: Conceptualization, Methodology, Writing - review & editing.

*Competing interests.* The authors declare no competing interests.

535 *Acknowledgements.* The research described in this paper was performed at the Jet Propulsion Laboratory, California Institute of Technology, under contract with NASA. The authors thank Pulong Ma and Chris O'Dell for helpful guidance.

## Appendix A: Closed Form Jacobians

To obtain a closed for equation for the Jacobians used in the XCO<sub>2</sub> retrievals, we must explicitly compute the term  $\frac{d}{dx^*}\Gamma(\mathbf{x}^*, \mathbf{X})$  in equation (3). To accomplish this, we compute the partial derivative of the kernel function (4) wrt. the first input:

$$540 \quad \frac{\partial}{\partial \mathbf{x}} k(\mathbf{x}, \mathbf{x}') = \frac{\partial}{\partial \mathbf{x}} \left[ \alpha_1 \left( 1 + \frac{\sqrt{3}}{l} \|(\mathbf{x} - \mathbf{x}')\|_{\mathcal{W}} \right) \exp \left( -\frac{\sqrt{3}}{l} \|(\mathbf{x} - \mathbf{x}')\|_{\mathcal{W}} \right) + \alpha_2 (\mathcal{W}\mathbf{x})^T (\mathcal{W}\mathbf{x}') \right] \quad (\text{A1})$$

$$= \frac{\partial}{\partial \mathbf{x}} \left[ \alpha_1 \exp \left( -\frac{\sqrt{3}}{l} \|(\mathbf{x} - \mathbf{x}')\|_{\mathcal{W}} \right) \right] + \frac{\partial}{\partial \mathbf{x}} \left[ \alpha_1 \left( \frac{\sqrt{3}}{l} \|(\mathbf{x} - \mathbf{x}')\|_{\mathcal{W}} \right) \exp \left( -\frac{\sqrt{3}}{l} \|(\mathbf{x} - \mathbf{x}')\|_{\mathcal{W}} \right) \right] \quad (\text{A2})$$

$$+ \frac{\partial}{\partial \mathbf{x}} [\alpha_2 (\mathcal{W}\mathbf{x})^T (\mathcal{W}\mathbf{x}')] \quad (\text{A3})$$

$$= \frac{\partial \mathbf{d}}{\partial \mathbf{x}} \frac{\partial}{\partial \mathbf{d}} \left[ \alpha_1 \exp \left( -\frac{\sqrt{3}}{l} \mathbf{d} \right) \right] + \frac{\partial \mathbf{d}}{\partial \mathbf{x}} \frac{\partial}{\partial \mathbf{d}} \left[ \alpha_1 \left( \frac{\sqrt{3}}{l} \mathbf{d} \right) \exp \left( -\frac{\sqrt{3}}{l} \mathbf{d} \right) \right] + \frac{\partial}{\partial \mathbf{x}} [\alpha_2 (\mathcal{W}\mathbf{x})^T (\mathcal{W}\mathbf{x}')] \quad (\text{A4})$$

$$= \frac{\partial \mathbf{d}}{\partial \mathbf{x}} \left[ -\alpha_1 \left( \frac{\sqrt{3}}{l} \right) \exp \left( -\frac{\sqrt{3}}{l} \mathbf{d} \right) \right] + \frac{\partial \mathbf{d}}{\partial \mathbf{x}} \left[ \alpha_1 \left( \frac{\sqrt{3}}{l} \right) \exp \left( -\frac{\sqrt{3}}{l} \mathbf{d} \right) - \alpha_1 \left( \frac{\sqrt{3}}{l} \right)^2 \mathbf{d} \exp \left( -\frac{\sqrt{3}}{l} \mathbf{d} \right) \right] \quad (\text{A5})$$

$$545 \quad + [\alpha_2 (\mathcal{W})^T (\mathcal{W}\mathbf{x}')] \quad (\text{A6})$$

$$= \frac{\partial \mathbf{d}}{\partial \mathbf{x}} \left[ -\alpha_1 \left( \frac{\sqrt{3}}{l} \right)^2 \mathbf{d} \exp \left( -\frac{\sqrt{3}}{l} \mathbf{d} \right) \right] + [\alpha_2 (\mathcal{W})^T (\mathcal{W}\mathbf{x}')] \quad (\text{A7})$$

$$= \frac{\mathcal{W}(\mathcal{W}(\mathbf{x} - \mathbf{x}'))}{\mathbf{d}} \left[ -\alpha_1 \left( \frac{\sqrt{3}}{l} \right)^2 \mathbf{d} \exp \left( -\frac{\sqrt{3}}{l} \mathbf{d} \right) \right] + [\alpha_2 (\mathcal{W})^T (\mathcal{W}\mathbf{x}')] \quad (\text{A8})$$

$$= \mathcal{W}^2 \left[ -\alpha_1 \left( \frac{\sqrt{3}}{l} \right)^2 \exp \left( -\frac{\sqrt{3}}{l} \|(\mathbf{x} - \mathbf{x}')\|_{\mathcal{W}} \right) (\mathbf{x} - \mathbf{x}') + \alpha_2 \mathbf{x}' \right] \quad (\text{A9})$$

After computing  $\frac{\partial}{\partial \mathbf{x}} k(\mathbf{x}, \mathbf{x}')$ , we get  $\frac{d}{dx^*}\Gamma(\mathbf{x}^*, \mathbf{X})$  element-by-element with  $\mathbf{x}$  being the new input and  $\mathbf{x}'$  a training data  
550 point. The final Jacobian is then obtained by computing  $\frac{d}{dx^*}z^*$  via (3) and reversing transformations (19) and (20).

## References

- Battle, P., Darcy, M., Hosseini, B., and Owhadi, H.: Kernel Methods are Competitive for Operator Learning, 2023.
- Boesch, H., Brown, L., Castano, R., Christi, M., Connor, B., Crisp, D., Eldering, A., Fisher, B., Frankenberg, C., Gunson, M., Granat, R., McDuffie, J., Miller, C., Natraj, V., O'Brien, D., O'Dell, C., Osterman, G., Oyafuso, F., Payne, V., Polonski, I., Smyth, M., Spurr, R., Thompson, D., and Toon, G.: Orbiting Carbon Observatory-2 (OCO-2) Level 2 Full Physics Retrieval Algorithm Theoretical Basis, Version 2.0 Rev 2, 2015.
- Braverman, A., Hobbs, J., Teixeira, J., and Gunson, M.: Post hoc Uncertainty Quantification for Remote Sensing Observing Systems, *SIAM/ASA J. Uncertain. Quantification*, 9, 1064–1093, <https://doi.org/10.1137/19M1304283>, 2021.
- Bréon, F.-M., David, L., Chatelana, P., and Chevallier, F.: On the potential of a neural-network-based approach for estimating XCO<sub>2</sub> from OCO-2 measurements, *Atmospheric Measurement Techniques*, 15, 5219–5234, <https://doi.org/10.5194/amt-15-5219-2022>, 2022.
- Brynjarsdóttir, J., Hobbs, J., Braverman, A., and Mandrake, L.: Optimal Estimation Versus MCMC for CO<sub>2</sub> Retrievals, *Journal of Agricultural, Biological and Environmental Statistics*, 23, 297–316, <https://doi.org/10.1007/s13253-018-0319-8>, 2018.
- Byrne, B., Baker, D. F., Basu, S., Bertolacci, M., Bowman, K. W., Carroll, D., Chatterjee, A., Chevallier, F., Ciais, P., Cressie, N., Crisp, D., Crowell, S., Deng, F., Deng, Z., Deutscher, N. M., Dubey, M., Feng, S., García, O., Griffith, D. W. T., Herkommer, B., Hu, L., Jacobson, A. R., Janardanan, R., Jeong, S., Johnson, M. S., Jones, D. B. A., Kivi, R., Liu, J., Liu, Z., Maksyutov, S., Miller, J. B., Miller, S. M., Morino, I., Notholt, J., Oda, T., O'Dell, C. W., Oh, Y.-S., Ohyama, H., Patra, P. K., Peiro, H., Petri, C., Philip, S., Pollard, D. F., Poulter, B., Remaud, M., Schuh, A., Sha, M. K., Shiomi, K., Strong, K., Sweeney, C., Té, Y., Tian, H., Velasco, V. A., Vrekoussis, M., Warneke, T., Worden, J. R., Wunch, D., Yao, Y., Yun, J., Zammit-Mangion, A., and Zeng, N.: National CO<sub>2</sub> budgets (2015–2020) inferred from atmospheric CO<sub>2</sub> observations in support of the Global Stocktake, *Earth System Science Data Discussions*, 2022, 1–59, <https://doi.org/10.5194/essd-2022-213>, 2022.
- Chevallier, F., Ciais, P., Conway, T. J., Aalto, T., Anderson, B. E., Bousquet, P., Brunke, E. G., Ciattaglia, L., Esaki, Y., Frohlich, M., Gomez, A., Gomez-Pelaez, A. J., Haszpra, L., Krummel, P., Langenfelds, R. L., Leuenberger, M., Machida, T., Maignan, F., Matsueda, H., Morgu, J. A., Mukai, H., Nakazawa, T., Peylin, P., Ramonet, M., Rivier, L., Sawa, Y., Schmidt, M., Steele, L. P., Vay, S. A., Vermeulen, A. T., Wofsy, S., , and Worthy, D.: CO<sub>2</sub> surface fluxes at grid point scale estimated from a global 21 year re-analysis of atmospheric measurements, *J. Geophys. Res. Atmos.*, <https://doi.org/https://doi.org/10.1029/2010JD013887>, 2010.
- Connor, B. J., Boesch, H., Toon, G., Sen, B., Miller, C., and Crisp, D.: Orbiting Carbon Observatory: Inverse Method and Prospective Error Analysis, *J. Geophys. Res.*, 113, D05305, <https://doi.org/10.1029/2006JD008336>, 2008.
- Cressie, N.: *Statistics for Spatial Data*, John Wiley & Sons, Inc., 1993.
- Cressie, N.: Mission CO<sub>2</sub>ntrol: A Statistical Scientist's Role in Remote Sensing of Atmospheric Carbon Dioxide, *Journal of the American Statistical Association*, 113, 152–168, <https://doi.org/10.1080/01621459.2017.1419136>, 2018.
- Crisp, D., Atlas, R. M., Breon, F.-M., Brown, L. R., Burrows, J. P., Ciais, P., Connor, B. J., Doney, S. C., Fung, I. Y., Jacob, D. J., Miller, C. E., O'Brien, D., Pawson, S., Randerson, J. T., Rayner, P., Salawitch, R. J., Sander, S. P., Sen, B., Stephens, G. L., Tans, P. P., Toon, G. C., Wennberg, P. O., et al.: The Orbiting Carbon Observatory (OCO) mission, *Adv. Space. Res.*, 34, 700–709, <https://doi.org/10.1016/j.asr.2003.08.062>, 2004.
- Crisp, D., Fisher, B. M., O'Dell, C., Frankenberg, C., Basilio, R., Bösch, H., Brown, L. R., Castano, R., Connor, B., Deutscher, N. M., Eldering, A., Griffith, D., Gunson, M., Kuze, A., Mandrake, L., McDuffie, J., Messerschmidt, J., Miller, C. E., Morino, I., Natraj, V., Notholt, J., O'Brien, D. M., Oyafuso, F., Polonsky, I., Robinson, J., Salawitch, R., Sherlock, V., Smyth, M., Suto, H., Taylor, T. E., Thompson,

- D. R., Wennberg, P. O., Wunch, D., and Yung, Y. L.: The ACOS CO<sub>2</sub> retrieval algorithm; Part II: Global XCO<sub>2</sub> data characterization, *Atmospheric Measurement Techniques*, 5, 687–707, <https://doi.org/10.5194/amt-5-687-2012>, 2012.
- 590 Crisp, D., Pollock, H. R., Rosenberg, R., Chapsky, L., Lee, R. A. M., Oyafuso, F. A., Frankenberg, C., O'Dell, C. W., Bruegge, C. J., Doran, G. B., Eldering, A., Fisher, B. M., Fu, D., Gunson, M. R., Mandrake, L., Osterman, G. B., Schwandner, F. M., Sun, K., Taylor, T. E., Wennberg, P. O., and Wunch, D.: The On-orbit Performance of the Orbiting Carbon Observatory-2 (OCO-2) Instrument and its Radiometrically Calibrated Products, *Atmos. Meas. Tech.*, 10, 59–81, <https://doi.org/10.5194/amt-10-59-2017>, 2017.
- Crisp, D., O'Dell, C., Eldering, A., Fisher, B., Oyafuso, F., Payne, V., Drouin, B., Toon, G., Laughner, J., Somkuti, P., McGarragh, G., 595 Merrelli, A., Nelson, R., Gunson, M., Frankenberg, C., Osterman, G., Boesch, H., Brown, L., Castano, R., Christi, M., Connor, B., McDuffie, J., Miller, C., Natraj, V., O'Brien, D., Polonski, I., Smyth, M., Thompson, D., and Granat, R.: Orbiting Carbon Observatory-2 & 3 (OCO-2 & OCO-3) Level 2 Full Physics Retrieval Algorithm Theoretical Basis, Version 3.0, 2021.
- Crowell, S., Baker, D., Schuh, A., Basu, S., Jacobson, A. R., Chevallier, F., Liu, J., Deng, F., Feng, L., McKain, K., Chatterjee, A., Miller, J. B., Stephens, B. B., Eldering, A., Crisp, D., Schimel, D., Nassar, R., O'Dell, C. W., Oda, T., Sweeney, C., Palmer, P. I., and Jones, 600 D. B. A.: The 2015–2016 carbon cycle as seen from OCO-2 and the global in situ network, *Atmospheric Chemistry and Physics*, 19, 9797–9831, <https://doi.org/10.5194/acp-19-9797-2019>, 2019.
- Datta, A., Banerjee, S., Finley, A., and Gelfand, A.: Hierarchical Nearest-Neighbor Gaussian Process Models for Large Geostatistical Datasets, *J Am Stat Assoc*, <https://doi.org/10.1080/01621459.2015.1044091>, 2016.
- David, L., Breon, F. M., and Chevallier, F.: XCO<sub>2</sub> estimates from the OCO-2 measurements using a neural network approach, *Atmospheric 605 Measurement Techniques*, 14, 117–132, <https://doi.org/10.5194/AMT-14-117-2021>, 2021.
- Eldering, A., Taylor, T. E., O'Dell, C. W., and Pavlick, R.: The OCO-3 Mission: Measurement Objectives and Expected Performance Based on 1 Year of Simulated Data, *Atmos. Meas. Tech.*, 12, 2341–2370, <https://doi.org/10.5194/amt-12-2341-2019>, 2019.
- Frey, M., Sha, M. K., Hase, F., Kiel, M., Blumenstock, T., Harig, R., Surawicz, G., Deutscher, N. M., Shiomi, K., Franklin, J. E., Bösch, H., Chen, J., Grutter, M., Ohyama, H., Sun, Y., Butz, A., Mengistu Tsidu, G., Ene, D., Wunch, D., Cao, Z., Garcia, O., Ramonet, M., Vogel, F., and Orphal, J.: Building the Collaborative Carbon Column Observing Network (COCCON): long-term stability and ensemble performance of the EM27/SUN Fourier transform spectrometer, *Atmospheric Measurement Techniques*, 12, 1513–1530, <https://doi.org/10.5194/amt-12-1513-2019>, 2019.
- Friedlingstein, P., Meinshausen, M., Arora, V., Jones, C., Anav, A., Liddicoat, S., and Knutti, R.: Uncertainties in CMIP5 Climate Projections due to Carbon Cycle Feedbacks, *Journal of Climate*, 27, <https://doi.org/10.1175/JCLI-D-12-00579.1>, 2014.
- 615 Friedlingstein, P., O'sullivan, M., Jones, M. W., Andrew, R. M., Gregor, L., Hauck, J., Quéré, C. L., Luijkx, I. T., Olsen, A., Peters, G. P., Peters, W., Pongratz, J., Schwingshackl, C., Sitch, S., Canadell, J. G., Ciais, P., Jackson, R. B., Alin, S. R., Alkama, R., Arneeth, A., Arora, V. K., Bates, N. R., Becker, M., Bellouin, N., Bittig, H. C., Bopp, L., Chevallier, F., Chini, L. P., Cronin, M., Evans, W., Falk, S., Feely, R. A., Gasser, T., Gehlen, M., Gkritzalis, T., Gloege, L., Grassi, G., Gruber, N., Özgür Gürses, Harris, I., Hefner, M., Houghton, R. A., Hurtt, G. C., Iida, Y., Ilyina, T., Jain, A. K., Jersild, A., Kadono, K., Kato, E., Kennedy, D., Goldewijk, K. K., Knauer, J., Korsbakken, J. I., 620 Landschützer, P., Lefèvre, N., Lindsay, K., Liu, J., Liu, Z., Marland, G., Mayot, N., Mcgrath, M. J., Metz, N., Monacci, N. M., Munro, D. R., Nakaoka, S. I., Niwa, Y., O'brien, K., Ono, T., Palmer, P. I., Pan, N., Pierrot, D., Pocock, K., Poulter, B., Resplandy, L., Robertson, E., Rödenbeck, C., Rodriguez, C., Rosan, T. M., Schwinger, J., Séférian, R., Shutler, J. D., Skjelvan, I., Steinhoff, T., Sun, Q., Sutton, A. J., Sweeney, C., Takao, S., Tanhua, T., Tans, P. P., Tian, X., Tian, H., Tilbrook, B., Tsujino, H., Tubiello, F., Werf, G. R. V. D., Walker, A. P., Wanninkhof, R., Whitehead, C., Wranne, A. W., Wright, R., Yuan, W., Yue, C., Yue, X., Zaehle, S., Zeng, J., and Zheng, B.: Global 625 Carbon Budget 2022, *Earth System Science Data*, 14, 4811–4900, <https://doi.org/10.5194/ESSD-14-4811-2022>, 2022.

- Gurney, K., Law, R., Denning, A., Rayner, P., Baker, D., Bousquet, P., Bruhwiler, L., Chen, Y., Ciais, P., Fan, S., Fung, I., Gloor, M., Heimann, M., Higuchi, K., John, J., Maki, T., Maksyutov, S., Masarie, K., Peylin, P., Prather, M., Pak, B., Randerson, J., Sarmiento, J., Taguchi, S., Takahashi, T., and Yuen, C. a.: Towards robust regional estimates of CO<sub>2</sub> sources and sinks using atmospheric transport models, *Nature*, <https://doi.org/10.1038/415626a>, 2002.
- 630 Hobbs, J., Braverman, A., Cressie, N., Granat, R., and Gunson, M.: Simulation-Based Uncertainty Quantification for Estimating Atmospheric CO<sub>2</sub> from Satellite Data, *SIAM/ASA Journal on Uncertainty Quantification*, 5, 956–985, <https://doi.org/10.1137/16M1060765>, 2017.
- Hobbs, J., Katzfuss, M., Zilber, D., Brynjarsdóttir, J., Mondal, A., and Berrocal, V.: Spatial Retrievals of Atmospheric Carbon Dioxide from Satellite Observations, *Remote Sensing*, 13, <https://doi.org/10.3390/rs13040571>, 2021.
- Imasu, R., Matsunaga, T., Nakajima, M., Yoshida, Y., Shiomi, K., Morino, I., Saitoh, N., Niwa, Y., Someya, Y., Oishi, Y., Hashimoto, M., Noda, H., Hikosaka, K., Uchino, O., Maksyutov, S., Takagi, H., Ishida, H., Nakajima, T. Y., Nakajima, T., and Shi, C.: Greenhouse gases Observing SATellite 2 (GOSAT-2): mission overview, *Prog Earth Planet Sci*, 10, <https://doi.org/https://doi.org/10.1186/s40645-023-00562-2>, 2023.
- 635 Innes, M.: Don't Unroll Adjoint: Differentiating SSA-Form Programs, *CoRR*, abs/1810.07951, <http://arxiv.org/abs/1810.07951>, 2018.
- IPCC: Summary for Policymakers, p. 1–34, IPCC, <https://doi.org/10.1017/CBO9781107415324.004>, 2023.
- 640 Johnson, S. G.: The Sobol module for Julia, <https://github.com/JuliaMath/Sobol.jl>, 2020.
- Kaipio, J. and Somersalo, E.: *Statistical and Computational Inverse Problems*, Springer, 2005.
- Kalnay, E.: *Atmospheric Modeling, Data Assimilation and Predictability*, Cambridge University Press, 2002.
- Kasahara, M., Kachi, M., Inaoka, K., Fujii, H., Kubota, T., Shimada, R., and Kojima, Y.: Overview and current status of GOSAT-GW mission and AMSR3 instrument, in: *Sensors, Systems, and Next-Generation Satellites XXIV*, edited by Neeck, S. P., Hélière, A., and Kimura, T., vol. 11530, p. 1153007, International Society for Optics and Photonics, SPIE, <https://doi.org/10.1117/12.2573914>, 2020.
- 645 Kiel, M., O'Dell, C. W., Fisher, B., Eldering, A., Nassar, R., MacDonald, C. G., and Wennberg, P. O.: How bias correction goes wrong: measurement of XCO<sub>2</sub> affected by erroneous surface pressure estimates, <https://doi.org/10.5194/amt-12-2241-2019>, 2019.
- Kingma, D. P. and Ba, J.: *Adam: A Method for Stochastic Optimization*, 2017.
- Kuze, A., Suto, H., Nakajima, M., and Hamazaki, T.: Thermal and near infrared sensor for carbon observation Fourier-transform spectrometer on the Greenhouse Gases Observing Satellite for greenhouse gases monitoring, *Appl. Opt.*, 48, 6716–6733, <https://doi.org/10.1364/AO.48.006716>, 2009.
- 650 Lamminpää, O.: Forward Model Emulator for Atmospheric Radiative Transfer Using Gaussian Processes And Cross Validation, [osf.io/u2t8a](https://osf.io/u2t8a), 2024.
- Lamminpää, O., Hobbs, J., Brynjarsdóttir, J., Laine, M., Braverman, A., Lindqvist, H., and Tamminen, J.: Accelerated MCMC for Satellite-Based Measurements of Atmospheric CO<sub>2</sub>, *Remote Sensing*, 11, <https://doi.org/10.3390/rs11172061>, 2019.
- 655 Li, Z., Huang, D. Z., Liu, B., and Anandkumar, A.: Fourier Neural Operator with Learned Deformations for PDEs on General Geometries, 2022.
- Liu, J., Bowman, K. W., Schimel, D. S., Parazoo, N. C., Jiang, Z., Lee, M., Bloom, A. A., Wunch, D., Frankenberg, C., Sun, Y., O'Dell, C. W., Gurney, K. R., Menemenlis, D., Gierach, M., Crisp, D., and Eldering, A.: Contrasting carbon cycle responses of the tropical continents to the 2015–2016 El Niño, *Science*, 358, <https://doi.org/10.1126/science.aam5690>, 2017.
- 660 Lu, L., Jin, P., Pang, G., Zhang, Z., and Karniadakis, G. E.: Learning nonlinear operators via DeepONet based on the universal approximation theorem of operators, *Nature Machine Intelligence*, 3, 218–229, <https://doi.org/10.1038/s42256-021-00302-5>, 2021.



- Ma, P., Mondal, A., Konomi, B. A., Hobbs, J., Song, J. J., and Kang, E. L.: Computer Model Emulation with High-Dimensional Functional Output in Large-Scale Observing System Uncertainty Experiments, *Technometrics*, 64, 65–79, 665 <https://doi.org/10.1080/00401706.2021.1895890>, 2019.
- McDuffie, J., Bowman, K. W., Hobbs, J., Natraj, V., Val, S., Sarkissian, E., and Thill, M. D.: ReFRACtor: Reusable Software Framework for Retrieval of Satellite Atmospheric Composition, in: *AGU Fall Meeting Abstracts*, vol. 2018, pp. A11F–2282, <https://github.com/ReFRACtor/>, 2018.
- Mishra, S. and Molinaro, R.: Physics informed neural networks for simulating radiative transfer, *Journal of Quantitative Spectroscopy and Radiative Transfer*, 270, 107 705, <https://doi.org/10.1016/J.JQSRT.2021.107705>, 2021. 670
- Moore III, B., Crowell, S. M. R., Rayner, P. J., Kumer, J., O’Dell, C. W., O’Brien, D., Utembe, S., Polonsky, I., Schimel, D., and Lemen, J.: The Potential of the Geostationary Carbon Cycle Observatory (GeoCarb) to Provide Multi-scale Constraints on the Carbon Cycle in the Americas, *Front. Environ. Sci.*, 17, 6, <https://doi.org/10.3389/fenvs.2018.00109>, 2018.
- Nguyen, H. and Hobbs, J.: Intercomparison of Remote Sensing Retrievals: An Examination of Prior-Induced Biases in Averaging Kernel Corrections, *Remote Sensing*, 12, <https://doi.org/10.3390/rs12193239>, 2020. 675
- O’Dell, C. W., Connor, B., Bosch, H., O’Brien, D., Frankenberg, C., Castano, R., Christi, M., Eldering, D., Fisher, B., Gunson, M., McDuffie, J., Miller, C. E., Natraj, V., Oyafuso, F., Polonsky, I., Smyth, M., Taylor, T., Toon, G. C., Wennberg, P. O., and Wunch, D.: The ACOS CO<sub>2</sub> Retrieval Algorithm - Part 1: Description and Validation Against Synthetic Observations, *Atmos. Meas. Tech.*, 5, 99–121, <https://doi.org/10.5194/amt-5-99-2012>, 2012.
- O’Dell, C. W., Eldering, A., Wennberg, P. O., Crisp, D., Gunson, M. R., Fisher, B., Frankenberg, C., Kiel, M., Lindqvist, H., Mandrake, L., Nelson, A. M. V. N. R. R., Payne, G. B. O. V. H., Taylor, T. E., Wunch, D., Drouin, B. J., Smyth, F. O. A. C. J. M. M., Baker, D. F., Basu, S., Feng, F. C. S. M. R. C. L., Palmer, P. I., García, M. D. O. E., Griffith, D. W. T., Hase, F., Iraci, L. T., Kivi, R., Morino, I., Notholt, J., Petri, H. O. C., Roeh, C. M., Sha, M. K., Strong, K., Te, R. S. Y., Uchino, O., and Velazco, V. A.: Improved Retrievals of Carbon Dioxide from Orbiting Carbon Observatory-2 with the Version 8 ACOS algorithm, *Atmos. Meas. Tech.*, 11, 6539–6576, <https://doi.org/10.5194/amt-11-6539-2018>, 2018. 680 685
- Owhadi, H. and Yoo, G. R.: Kernel Flows: From learning kernels from data into the abyss, *Journal of Computational Physics*, 389, 22–47, <https://doi.org/https://doi.org/10.1016/j.jcp.2019.03.040>, 2019.
- Palmer, P. I., Feng, L., Baker, D., Chevallier, F., Bösch, H., and Somkuti, P.: Net carbon emissions from African biosphere dominate pan-tropical atmospheric CO<sub>2</sub> signal, *Nature Communications*, 10, 3344, <https://doi.org/10.1038/s41467-019-11097-w>, 2019.
- Patil, P., Kuusela, M., and Hobbs, J.: Objective Frequentist Uncertainty Quantification for Atmospheric CO<sub>2</sub> Retrievals, *SIAM/ASA Journal on Uncertainty Quantification*, 10, 827–859, <https://doi.org/10.1137/20M1356403>, 2022. 690
- Patra, P., Crisp, D., Kaiser, J., Wunch, D., Saeki, T., Ichii, K., , Sekiya, T., Wennberg, P., Feist, D., Pollard, D., Griffith, D., Velazco, V., Maziere, M., Sha, M., Roehl, C., Chatterjee, A., and Ishijima, K.: The Orbiting Carbon Observatory (OCO-2) tracks 2–3 peta-gram increase in carbon release to the atmosphere during the 2014–2016 El Niño, *Sci Rep*, 7, <https://doi.org/https://doi.org/10.1038/s41598-017-13459-0>, 2007. 695
- Peiro, H., Crowell, S., Schuh, A., Baker, D. F., O’Dell, C., Jacobson, A. R., Chevallier, F., Liu, J., Eldering, A., Crisp, D., Deng, F., Weir, B., Basu, S., Johnson, M. S., Philip, S., and Baker, I.: Four years of global carbon cycle observed from the Orbiting Carbon Observatory 2 (OCO-2) version 9 and in situ data and comparison to OCO-2 version 7, *Atmospheric Chemistry and Physics*, 22, 1097–1130, <https://doi.org/10.5194/acp-22-1097-2022>, 2022.

- 700 Peters, W., Jacobson, A. R., Sweeney, C., Andrews, A. E., Conway, T. J., Masarie, K., Miller, J. B., Bruhwiler, L. M. P., Pétron, G., Hirsch, A. I., Worthy, D. E. J., van der Werf, G. R., Randerson, J. T., Wennberg, P. O., Krol, M. C., and Tans, P. P.: An Atmospheric Perspective on North American Carbon Dioxide Exchange: CarbonTracker, *Proc. Natl. Acad. Sci.*, 104, 18925–18930, <https://doi.org/10.1073/pnas.07089861>, 2007.
- Press, W. H., Flannery, B. P., Teukolsky, S. A., and Vetterling, W. T.: *Numerical Recipes in FORTRAN 77: The Art of Scientific Computing*, Cambridge University Press, 2 edn., <http://www.worldcat.org/isbn/052143064X>, 1992.
- 705 Ran, Y. and Li, X.: TanSat: a new star in global carbon monitoring from China, *Science Bulletin*, 64, 284–285, <https://doi.org/https://doi.org/10.1016/j.scib.2019.01.019>, 2019.
- Rasmussen, C. and Williams, C.: *Gaussian Processes for Machine Learning*, Adaptive Computation and Machine Learning, MIT Press, Cambridge, MA, USA, <http://gaussianprocess.org/gpml/>, 2006.
- 710 Rodgers, C. D.: *Inverse Methods for Atmospheric Sounding: Theory and Practice*, World Scientific Publishing Co. Pte. Ltd., 5 Toh Tuck Link, Singapore 596224, reprint edn., 2004.
- Rosenberg, R., Maxwell, S., Johnson, B. C., Chapsky, L., Lee, R. A. M., and Pollock, R.: Preflight Radiometric Calibration of Orbiting Carbon Observatory 2, *IEEE Trans. Geosci. Remote Sens.*, 55, 1994–2006, <https://doi.org/10.1109/TGRS.2016.2634023>, 2017.
- Schimel, D., Pavlick, R., Fisher, J. B., Asner, G. P., Saatchi, S., Townsend, P., Miller, C., Frankenberg, C., Hibbard, K.,  
715 , and Cox, P.: Observing terrestrial ecosystems and the carbon cycle from space, *Glob. Change Biol.*, pp. 1762—1776, <https://doi.org/https://doi.org/10.1111/gcb.12822>, 2015.
- Sierk, B., Be'zy, J.-L., Lo'scher, A., and Meijer, Y.: The European CO<sub>2</sub> Monitoring Mission: observing anthropogenic greenhouse gas emissions from space, in: *International Conference on Space Optics — ICSO 2018*, edited by Sodnik, Z., Karafolas, N., and Cugny, B., vol. 11180, p. 11180M, International Society for Optics and Photonics, SPIE, <https://doi.org/10.1117/12.2535941>, 2019.
- 720 Sobol, I.: Distribution of Points in a Cube and Approximate Evaluation of Integrals, *Zh. Vych. Mat. Mat. Fiz.*, 7, 784–802, 1967.
- Stein, M. L.: *Interpolation of spatial data: some theory for kriging*, Springer Science & Business Media, 1999.
- Stewart, G. W.: *Matrix algorithms, volume I*, SIAM, Society for industrial and applied mathematics, 1998.
- Tukiainen, S., Railo, J., Laine, M., Hakkarainen, J., Kivi, R., Heikkinen, P., Chen, H., and Tamminen, J.: Retrieval of atmospheric CH<sub>4</sub> profiles from Fourier transform infrared data using dimension reduction and MCMC, *Journal of Geophysical Research: Atmospheres*,  
725 121, 10,312–10,327, <https://doi.org/https://doi.org/10.1002/2015JD024657>, 2016.
- Turmon, M. and Braverman, A.: Uncertainty quantification for JPL retrievals, *Tech. rep.*, <https://doi.org/2014/45978>, 2019.
- Vecchia, A. V.: Estimation and Model Identification for Continuous Spatial Processes, *Journal of the Royal Statistical Society. Series B (Methodological)*, 50, 297–312, <http://www.jstor.org/stable/2345768>, 1988.
- Veefkind, J., Aben, I., McMullan, K., Förster, H., de Vries, J., Otter, G., Claas, J., Eskes, H., de Haan, J., Kleipool, Q., van  
730 Weele, M., Hasekamp, O., Hoogeveen, R., Landgraf, J., Snel, R., Tol, P., Ingmann, P., Voors, R., Kruizinga, B., Vink, R., Visser, H., and Levelt, P.: TROPOMI on the ESA Sentinel-5 Precursor: A GMES mission for global observations of the atmospheric composition for climate, air quality and ozone layer applications, *Remote Sensing of Environment*, 120, 70–83, <https://doi.org/https://doi.org/10.1016/j.rse.2011.09.027>, the Sentinel Missions - New Opportunities for Science, 2012.
- Wu, K., Yang, D., Liu, Y., Cai, Z., Zhou, M., Feng, L., and Palmer, P. I.: Evaluating the Ability of the Pre-Launch TanSat-2 Satellite to  
735 Quantify Urban CO<sub>2</sub> Emissions, *Remote Sensing*, 15, <https://doi.org/10.3390/rs15204904>, 2023.
- Wunch, D., Wennberg, P. O., Osterman, G., Fisher, B., Naylor, B., Roehl, C. M., O'Dell, C., Mandrake, L., Viatte, C., Kiel, M., Griffith, D. W. T., Deutscher, N. M., Velazco, V. A., Notholt, J., Warneke, T., Petri, C., De Maziere, M., Sha, M. K., Sussmann, R., Rettinger, M.,

740 Pollard, D., Robinson, J., Morino, I., Uchino, O., Hase, F., Blumenstock, T., Feist, D. G., Arnold, S. G., Strong, K., Mendonca, J., Kivi, R., Heikkinen, P., Iraci, L., Podolske, J., Hillyard, P. W., Kawakami, S., Dubey, M. K., Parker, H. A., Sepulveda, E., García, O. E., Te, Y., Jeseck, P., Gunson, M. R., Crisp, D., and Eldering, A.: Comparisons of the Orbiting Carbon Observatory-2 (OCO-2) XCO<sub>2</sub> measurements with TCCON, *Atmospheric Measurement Techniques*, 10, 2209–2238, <https://doi.org/10.5194/amt-10-2209-2017>, 2017.

Zhu, X., Huang, L., Ibrahim, C., Lee, E. H., and Bindel, D.: Scalable Bayesian Transformed Gaussian Processes, 2022.